An experimental investigation on thermal striping.
Mixing phenomena of a non-buoyant jet with two adjacent buoyant jets as measured by ultrasound Doppler velocimetry

A. Tokuhiro

Reactor Engineering Section, Safety Engineering Division, Oarai Engineering Center
Power Reactor and Nuclear Fuel Development Corporation (PNC)
4002 Narita, Oarai-machi, Ibaraki-ken, Japan 311-13

Abstract Experiments were conducted to investigate the thermal mixing phenomena of three quasi-planar vertical jets, one unheated surrounded by two heated jets. Velocity measurements of a *reference* single-jet and the triple-jet configuration were taken by ultrasound Doppler velocimetry while temperature data were taken from 39 thermocouples traversed vertically. We found from a *hydrodynamic* perspective that beyond the exit region, our single-jet data behaved like previous single-jet data. In contrast the triple-jet exhibited for example, up to 20 times the root-mean-square velocity values in the downstream regions, especially in between the heated and unheated jets. In particular for equal jet exit velocities (3 jets), U_{avg}=0.5 m/s and a temperature difference between the jets, $\Delta T = T_{hot}$-$T_{cold} = 5°C$, we found that the convective mixing predominantly takes place at axial distances, $z/D_h = 2.0$ to 4.5, where D_h is the hydraulic diameter of the exit nozzle. Spanwise the mixing span a range, $x/D_h \sim 2.25$, centered about the unheated jet; that is, the region between the heated and unheated jets.

List of symbols

Symbol	Unit	
D_h	10^{-3} m	hydraulics diameter of the inlet channel
Gr	-----	Grashof number, $= (g\beta\Delta T\, z^3/v^2)$
L	10^{-3} m	length of the inlet channel
Pr	-----	Prandtl number, $= (v/\alpha)$
Re	-----	Reynolds number of inlet channel, $= (UD_h/v)$ or (Uz/v)
Ri	-----	Richardson number, $= Gr/Re^2$
$T_{hot}, T_{cold}, \Delta T, t'$	[°C]	temperature of heated, unheated jets, temperature difference between the two at the exit, root-mean-square of temperature
U_{avg}, U_o	10^{-3} m/s	characteristic velocity, velocity at the exit of the nozzle
$U_{ctr,max}$	10^{-3} m/s	maximum centerline velocity of the velocity profile
w'	10^{-3} m/s	root-mean-square velocity of w-component
x	10^{-3} m	transverse (cross-stream) coordinate
z, z_{uc}	10^{-3} m	axial coordinate as measured from jet exit and axial core length
α	m²/s	thermal diffusivity
β	1/K	coefficient of thermal expansion
v	m²/s	kinematic viscosity

1

Introduction

Thermal striping refers to random thermal cycling of reactor structures and components as a result of fluid-structure interaction; that is, striping is likely a description of the cold and hot (thermal) *stripes* or plumes and jets that a solid boundary must withstand due to *preferential or inefficient* mixing of typically coolant flowing through and exiting the core. The net result of this striping is undesirable since *thermal fatigue* of materials can lead to structural and material failure. Thermal striping as a phenomenological problem in LMFBRs was already recognized in the early 1980s by Wood (1980), Brunings (1982) and has subsequently been considered by Betts, Bourman and Sheriff (1983), Moriya et al. (1991) and in recent years by Muramatsu (1994).

We note here that, although the phenomena taken as a whole involve fluid-structure interaction, the analytical and experimental efforts have generally been divided into structural and thermal-hydraulic investigations. In the present work, we focus strictly on the thermal-hydraulic aspects; that is, mainly the convective mixing of a multiple number of jets at different temperatures. The number of jets can range from a single-jet, which has been most extensively studied, to two jets flowing side-by-side, at a relative angle or co-axially and with a relative velocity (and/or temperature) to each other. In fact co-axial jets of sodium have been investigated by Tenchine and Nam (1987) while Tenchine and Moro

(1995) compared the results of sodium and air jet experiments. Investigation of more than two jets seems to be rare. Thus besides its relevance to LMFBR thermal-hydraulics, a study of a multiple number of vertical jets at either the same or different densities (temperatures), may be of general interest to the heat transfer community.

In the present study, we carried out water-based experiments in a test facility simulating the mixing of one centrally located jet sandwiched by two adjacent and buoyant jets at higher (hotter) temperature. One objective of the study was to demonstrate the applicability of ultrasound Doppler velocimetry for velocity measurements. By applicability we mean velocity measurements in the flow field of relevance. Subsequently we first obtained and evaluated the hydrodynamic information concerning the nature of mixing between thermally-stratified jets. Then with the addition of temperature data we were able to assess the thermal-hydraulics of mixing.

2
Experiment
2.1 Experimental facility

Figure 1 shows the experimental loop including the test section. Except for the test section, the rest of the facility functions as a support system shared by two other experiments. The facility thus consists of the thermal striping test section set within a larger rectangular tank, a loop heater/exchanger for supplying hot water, a head tank in order to control the water-level, a filter to extract contaminants within the loop, an air-to-loop heat exchanger for supplying cold or cooled water back into the loop as well as a general purpose lab water supply tank. Several turbine flowmeters as well as orifice plate type devices, a system of valves and all the connecting piping are as depicted.

A more detailed view of the test section itself is shown in Figure 2. The test section is immersed within a rectangular tank measuring 2438W x 2438H x 671D [W-width, H-height, D-depth, all mm], and is itself a partially enclosed rectangular region measuring 400W x 950H x 176.5D. As noted in the top view, two acrylic plates sandwich the four rectangular blocks thereby restricting the spread of the exiting jets in these directions. The idea was to constrain the jet to a finite width and to "view" it as quasi two-dimensional within this geometry. The right and left sides are however, open so that even with overflow mechanism at the top of the test section there may be some recirculating flow through the sides. A prominent feature of the tank is the large viewing glass windows on both the *front, back* and *right side* of the tank. This feature was included primarily for laser-based measurements and flow visualization techniques. Below the test section are three rectangular channels defined by four equally rectangular blocks. The central channel functions as the "cold" jet while the adjacent two are "hot". The hot and cold jets are supplied from separate sources, the cold source being centrally situated, flowing first through an expansion and then through a flow constriction. The hot source is on the other hand supplied from the right-hand-side into a lower chamber. The flow then weaves its way past the

cold pipe and enters symmetrically through a one-sided rectangular constriction. The exit of the nozzle is a block elevated 75 mm from the reference *groundplane* of the tank.

The other prominent components of the test facility is the traversing thermocouple array and the UVP transducer holder fixed to the left arm of the traversing mechanism. A schematic is shown in Figure 3 along with the exit blocks. The moving mechanism consisted of two vertical and parallel pillars (OD 45mm), between which a "bridge" served as a mounting bracket for the thermocouples. This bridge is fixed and moves up and down with the pillars. The traversing thermocouple array consists of 39 thermocouples facing vertically downward and horizontally spaced 5 mm apart over a 190 mm span. The last 5 mm of each of 39 thermocouples are directly exposed to the flow, while beyond this point the T/C is insulated for a length of 50 mm. The T/Cs are threaded and bonded to an horizontal arm and contained either in the right or left arms. The two arms enter through the top of the rectangular tank. The thermocouple are T-type, constantan copper-nickel with an expected measurement error of 0.5°C. Operationally three T/Cs malfunctioned (No. 5, 6, 14 numbering from left) and could not be used for data acquisition.

Velocity measurements were taken using the Met-Flow Model X-1 Ultrasound Velocity Profile [UVP] (1992) monitor with a single, Delrin-encased (temperature limit ~ 80°C) piezo-electric transducer [TDX] operating at 4 MHz. The transducer had an active crystal diameter of 6 mm. The UVP works on the principle of ultrasound Doppler echography; that is, the position and velocity information are evaluated respectively from the detected time-of-flight and the Doppler-shift frequency at each of 128 locations. From these 128 locations, a componental velocity profile is constructed along the measurement line (ML) of the ultrasonic beam. By componental it is understood that the velocity vector oriented either toward or away from the face of the transducer (from the sign of the Doppler shift) and the magnitude is measured at each of the 128 "coin-like" volumetric elements during each of the 1024 measurement intervals. The real-time corresponding to 1024 measurement intervals is adjustable depending largely upon the preference (and experience) of the user, though it should be based on the phenomenon of interest in the flow; that is, based on estimates of the time-scales associated with various transport phenomena, the user is able to select either a short or long time span between measurements. The UVP can thus detect transient phenomena during a minimum time-span of 30 msec to minutes and hours. The device has been developed and tested most notably by Takeda (1986, 1991*a*, 1991*b*).

The ultrasound is reflected from tracer particles, typically a plastic powder with a nominal size of 50-100 μm ($\rho = 1.02$ kg/m^3), that are added to the test medium (water). One should note that the inherent assumptions in using this measurement technique are that: 1) the tracer particles accurately reflect the velocity profile of the liquid state and 2) the modification of the flow field due to addition of tracer particles; that is, the particle-to-fluid interaction, is of minor consequence to the measured profile.

Additionally, it is assumed that particle-to-particle interactions are negligible since the concentration of tracer particles, i.e. on the order of 100 grams per 4000 liters (3988) of water, is physically very low. Finally, regarding the former, we assume that there is no slip (relative) velocity between tracer particle and liquid; that is, the particle moves exactly as a fluid element would, as dictated by the initial and boundary conditions of the flow. As for the positioning of the transducer, it was held in place by a short piece of pipe through which the transducer was inserted (and held) and the output signal travels through a 4m long cable. The typical measurement time was of the order of 1-3 minutes.

2.2 Conditions of UVP and temperature measurements

For the data presented in this paper, the average exit velocity of both the single- and triple-jet experiments was 0.5 m/s with an estimated error of 0.1 m/s. The temperature difference between the cold and each of the hot jets was held to 5°C in all cases with an estimated error of 0.75°C. UVP measurements were conducted with the transducer fixed at either the right or left locations with respect to the jet(s) (see Figs. 2, 3). Measurements were taken axially, along the z-axis, at 5 mm intervals up to approximately 550 mm above the imaginary *"0"-plane* in most cases. For all the data present here, the UVP transducer was oriented at an angle of $10°$ with respect to the horizontal. The selection of the $10°$ angle was in reality an experimental compromise between a sufficient number of axial locations, which we sought in order to follow the flow development, and the detection of the larger, axial vector component relative to the horizontal component of the actual jetting flow.

3

Results

3.1 Photographs and Video Images

We first present in Figures 4 and 5 digitized image sequences of respectively, the single- and triple-jets extracted from video as a qualitative introduction. The images have been taken with laser-sheet (argon laser) illumination from the side with Rhodamine dye added to the test medium. An horizontal line tracing the laser sheet beam is clearly visible on the top surface of the 4 blocks. Since a normal speed video camera operating at 27 frames/sec was used the images of course missed flow phenomena too fast for it to record. Nevertheless, the single-jet, or rather an ideal planar jet, is said to consist of the following: 1) an *exit region*, which ideally has a *flat, square* or *top-hat* velocity profile but which of course depends on the upstream flow rectification, 2) a *mixing layer* or *developing region* where, as indicated in Figure 6, the mixing layer dynamics on both sides of the jet take place and the velocity profile changes, and 3) a *developed* or *self-preserved region* where the velocity profile is essentially *preserved* even as the jet disperses (widens) spatially. Additionally, one often mentions the *core flow* or *core* of the jet that describes the central region of the jet and additionally the *entrained flow* or *entrainment region*, which describes the flow that is swept into the jetting flow from the surrounding,

along the edge of the jet. Thus, it is clear that a turbulent planar jet would have both spatial (x, z) and temporal (time) dependence. Note that in the present set-up the axial coordinate is the z-axis and the spanwise or width-wise distance is the x-axis. Finally in order to facilitate our presentation, we refer to the buoyant jets as the "hot" jets and the non-buoyant, central jet as the "cold" jet.

3.2 UVP velocity profiles: Single-jet and Triple-jet

Figure 7a) shows a representative set of average velocity profiles of the single-jet taken by the UVP. The axial distances (z) have been chosen to clearly display the changes in the profile with downstream locations and thus represents the distance from the groundplane as indicated in Fig. 3. The abscissa depicts the 128 channels (0-127) along the ultrasound beam, a distance equivalent to 284 mm as noted. In Fig. 7b) we show one profile (z=45 mm) and its associated standard deviation profile in order to explain details of the profile itself. The actual profile as measured for example by the transducer depicted in Fig. 3 is the inverted image of Fig. 7b); that is, recall that with respect to the transducer, flows coming toward it are "--" (negative) and those flowing away are "+" with regard to the sign of the Doppler shift. This does not in any way change the information content of the depicted velocity profile. We thus see that a prominent feature is the peaked, jet-like profile in the central region. Additionally, to the sides of this central region are the entrained-flow regions which show flow of approximately equal magnitude and *on-average* of opposite sign with respect to the transducer. We say *on-average* here because the mixing layer-generated entrained flow dynamically changes direction and magnitude during the measurement period. We observed this while analyzing many sets of 1024 profiles per set of UVP velocity data. However, on average they are of opposite sign. We note that overall although narrower the velocity profile in Fig. 7b and in Fig. 6 are similar. Returning to Fig. 7a) we have artificially inverted the right-hand-side of the profile taken at z=45 and shown it as a dotted line to qualitatively illustrate the similarity with the developing jet depicted in Fig. 6. As for the standard deviation distribution the twin peaks and the valley in between appear to characterize the edge and core of the jet.

As a matter of comparison between our (isothermal) single-jet data with that from past investigations we show in Figure 8 the axial decay of the centerline velocity with those of investigators as noted. The data of past investigators have been extracted form Cheremisinoff (1986) and are represented by linear regression lines above the so-called velocity core length, z_{uc}. The core length corresponds to the axial point below which the data assumes a quasi-constant value ($z_{uc} \sim 4$). To the best of our knowledge the past data are for isothermal air jets. Note that there are variations in slope and magnitude even for identical fluids. Except for the exit region (z < 0.8) for which Cheremisinoff presents no data our data is consistent with past investigations.

176

Figure 9a) shows a representative set of average velocity profiles of the triple-jet at several coincidental axial locations as those in Fig. 7. Due in part to the number of jets (3) and the interaction between them the individual profiles are much more difficult to discern in this figure. We also include the profile near the maximum measured location, $z = 535$ mm, instead of at $z = 350$ and also provide data at $z = 195$. We next present in Fig. 9b) one profile and its associated standard deviation distribution at $z = 45$. The velocity profile taken here with the transducer at the right is clearly distorted, especially the left jet. The approximate location of the exit nozzles are indicated by triangular symbols on the x-axis. Note that similarly to Fig. 7b) the core and edges of each jets, certainly for the left and center jets are identifiable from the standard deviation profile. The left edge of the right jet is also evident. While details of the distorted profile are discussed later, we present respectively in Figs. 9c) and d) a composite triple-jet velocity profile and an idealized profile. The composite profile was constructed by taking one-half of the profiles from respectively the left and right transducer orientations and joining them at the center.

Figure 10 shows the calculated Root Mean Square (RMS) velocity distribution versus axial distance for both the single- and triple-jet, the latter for both left and right UVP transducer orientations. The triple-jet data were taken on two different occasions so that although operational conditions were nearly identical, it is likely that thermohydraulic conditions were not *exactly* reproduced. The single-jet data is for an isothermal jet. The average exit velocity in all three cases was 0.5 m/s. Figures 11a)-f) then show the estimated spanwise distribution (x-direction) of the ratio of the triple-jet RMS to that of the single-jet RMS with the axial location as the parameter. The data are shown in groups of four for clarity while for each type of jet, the RMS value has first been normalized by its own spanwise average velocity. The triple-to-single jet RMS ratio has been calculated at 8 spanwise regions, each containing velocity data (16 points) over a 35.5. mm span. Eight regions were selected since it was thought that a distribution consisting of 128 points would reveal fine detail not necessarily characteristic of the spanwise variation which might be revealed in a segment-wise average. Our objective was thus to qualitatively or semi-quantitatively reveal the difference in the normalized RMS distribution of the triple-jet versus the single-jet. After varying the number of regions we settled on 8 regions as representative of the spanwise variation.

3.3 Temperature data

The spanwise temperature distribution at selected axial locations is shown in Figure 12. Several points to the left are missing due to malfunctioning thermocouples. Each point represents a temperature averaged over ~ 20.5 seconds containing some 1025 samples. We note that the spatial resolution and span over which the velocity and temperature data were taken did not coincide; that is, the UVP data was taken over a length of 284 mm with a resolution of 2.21 mm whereas the thermocouples span 190 mm at 5 mm intervals. We mention this fact because it is of significance when combining velocity and temperature data. We next show in Figure 13 the corresponding spanwise distribution of the standard

deviation at selected axial stations. Compared to Fig. 11 the z-locations have here been selected to show the gradual change near the exit (z = 20, 30, 40 mm) and at or near the maximum magnitude (z = 120, 130, 140 mm) using Fig. 10 as a guide. Figure 14 is the temperature equivalent to Fig. 10 for velocity. Except that here we show the normalized RMS with the normalization factor being the spanwise averaged temperature.

Next in Figure 15 we show an iso-contour plot of the calculated turbulent heat flux distribution. The figure has been generated from separate calculations of w' and t', which respectively represent the velocity and temperature fluctuations as a function of (x,z). We have equated w' and t' to the RMS values as presented. Recall that the quantity w' is not strictly the z-component of velocity fluctuation since the UVP-TDX was oriented at 10° with respect to the horizontal; that is, it includes primarily the w' component but also a small contribution from u'. In addition since the traversed increments for temperature and velocity were of different sizes, some interpolation had to be performed in order to fill-in missing data. As a matter of approach, the *coarser* (larger traverse increments) temperature data was taken as the basis onto which the *finer* velocity data was adapted, so that interpolation would be minimized. Fortunately, both the temperature and velocity data have nearly equivalent *resolution* up to z ~ 275 (0 ~ x ~ 180), which also appears to be the region of relevance for thermal mixing. It is clear from the figure that beyond z ~ 300, the distribution shows largely *linear* patterns (straight lines) which are the result of sparsely recorded data points and interpolation between these points. We thus settled on a semi-quantitative presentation of the turbulent heat flux distribution.

Finally in Figure 16 we plot the frequency versus the axial distance of the first six peaks ordered in terms of "power" for the triple-jet. The frequencies were generated by applying a fast Fourier transform without any windows to the velocity profiles and characterize the hydrodynamic fluctuations inherent in our flow. They represent the fluctuations along the ultrasound beam. The ordering based on the power gives a measure of the turbulent kinetic energy associated with each frequency of the flow.

4

Discussion of results

4.1 UVP velocity profiles: Single-jet and Triple-jet

The images in Figs. 4 and 5 were presented to orient the reader and to facilitate the discussion to follow. A brief introduction regarding a way to view the UVP measured velocity profile was given based on single-jet data (Figs. 7). We subsequently verified that the our single-jet data, for example the centerline decay velocity was consistent with past experimental data (Fig. 8), even though most of the past data used air as the test medium. We then presented the average velocity and its associated standard deviation profiles for the triple-jet in Figs. 9a) and b).

In Fig. 9b) we note first that the jet exits are spanwise located along the abscissa at approximately x ~ 32, 64 and 96. The velocity profile taken at z = 45 (black symbol) show two slightly distorted peaks at the right and center but each with a shape similar to a single-jet profile. The profile corresponding to the right jet (x ~ 32), as taken from the right however, shows a distorted, twin-peaked shape. And although not shown, when taken from the left, the left jet showed a similarly distorted and twin-peaked profile. This inconsistency, that the distorted portion of the profile corresponds to the jet closest to the transducer, may be due to inadequate amplification of the echoes returning from the ultrasound wave reflecting tracer particles. That is, the linear amplification (versus distance from the transducer) which has been applied, although adequate for the distant channels (measurement volumes), appears insufficient for the (near) jetting region in question. The other distinct possibility is that due to the 10° orientation of the transducer, different axial segments of each jet is detected. As mentioned the 10° angle was in reality a compromise between including the contribution from the expectedly larger vertical component of velocity along the ultrasound beam (measuring line) to that of measuring as near identical axial segments (same z-locations) of the three jets as possible. In Fig. 9c) we have sketched the transducer at both right and left positions and also depict some of the just so-described details. Finally in Fig. 9d) we present a composite profile of the triple-jet with the left and right one-half portions taken with the transducer respectively from the right and left. The profile overlaps in channel number at the center and represents an undistorted profile of the triple-jet.

4.2 Comparison of triple-jet to single-jet velocity data

Fig. 10 depicts the axial distribution of the normalized *RMS* for both the single- and triple-jets, the latter for both right [R] and left [L] transducer orientations. While there are some differences in the triple-jet data the marked contrast is between the single- and triple-jets. In fact the triple-jet reaches values larger than what one might expect as a "rule-of-thumb"; that is, roughly three times the single-jet value (see $2 < z/D_h < 7$). Furthermore, the overall trend is different than the single-jet, which in comparison steadily increases up to $z/D_h \sim 11$ where it appears to reach a quasi-constant value. We note that in Gebhardt et al. (1988) the fully-turbulent region of an isothermal (or non-buoyant) axisymmetric jet, based on the axial distribution of the turbulent intensity, is reached at approximately 10 diameters downstream from the exit. If we can expect our quasi-planar jet to behave similarly then, for our average exit velocity-based Reynolds number of Re $\sim 2 \times 10^4$, our datum points have yet to reach a fully-turbulent state. Equally, that the peak intensity spans our measurement limit of $z/D_h \sim 15$ is different from the quoted work. The triple-jet in contrast, beyond a local minimum at $z/D_h \sim 1.2$, shows a rapid increase to a maximum value at $z/D_h \sim 6$ and thereafter an equally rapid decrease to a quasi-contant value at $z/D_h \sim 9$. From these data alone one could partially conclude that the "hydrodynamic" mixing of the hot and cold jets occurs within 2 to 10 diameters of the exit nozzle. By hydrodynamic we mean just based on velocity data while we acknowledge that the flow is thermal-hydraulic. Interestingly enough, beyond $z/D_h > 10$ the isothermal single-jet's RMS exceeds that of the

thermally-stratified triple-jet's. Since data of an isothermal triple-jet and/or a buoyant single-jet are not available at present we could not isolate nor fully assess the influence of (thermal) buoyancy on the turbulent mixing process. However, it does not appeal to physical reasoning that an isothermal triple-jet's RMS value would suddenly decrease to less than a single-jet's in comparison. So we believe it likely that either the energy content of the buoyant triple-jet is depleted due to thermal mixing and/or some form of turbulence suppression occurs; that is, something analogous to re-laminarization of turbulent mixed convective flows near the laminar-to-turbulent transition.

Since **Fig. 10** depicts the spanwise averaged RMS-values, it suppresses any details of the flow especially in-between the jets. We thus show in Fig. 11a)-to-f) the ratio of the normalized RMS of the triple jet to that of the single jet. Both the single- and triple-jet RMS-values are normalized by their respective spanwise average velocities. The thinking behind this particular way of data presentation was as follows. Since we are primarily interested in the convective mixing at the edge of each jet where potentially the largest temperature gradients are located, we do not necessarily need to look at the fine details of the spanwise velocity profile (for example Fig. 9a). In other words, even though this data is available, we know in advance some regions of interest of the triple-jet's configuration. Therefore, while we expect a fluctuating velocity signature within each of the 128 measurement volumes, we can afford to spatially average (or lump) the velocity level in segments; that is, we can spatially-average over a number of volumes and select the number of segments representative of the flow. Figs. 11a)-f) therefore show the triple-jet data taken from the right, normalized by the single-jet, also taken from the right-side. The legend in each figure shows the axial location at which the ratio was calculated. Since there was a discrepancy between single- and triple-jet measurement locations, a calculation of the RMS ratio at the same axial position was not always possible. Thus, where the locations differed, the axial locations are as noted.

It is clear from these plots that from $z \sim 70$ ($z/D_h \sim 1.96$) to about $z \sim 200$ ($z/D_h \sim 5.6$), the RMS of the triple-jet is larger (≥ 1) than that of the single-jet. In fact, between $95 \leq z \leq 120$ ($2.66 \leq z/D_h \leq 3.36$), the ratio can be as large as 20. Specifically the large values are reached typically in regions "3" and "6" which correspond respectively to the range $154.4 \leq x \leq 189.9$ mm and $225.4 \leq x \leq 260.9$ mm from the face of the transducer positioned at left (see Fig. 3). These regions substantially overlap the width of the two exit nozzle blocks located *in-between* the hot and cold jets. This gives strong support to localizing the thermalhydraulic mixing of our thermally-stratified jets. On the other hand, beyond $z \sim 300$ ($z/D_h \sim 8.39$), except for the left-most and right-most regions where the ratio is nearly one or slightly larger, the central region shows a value of less than one. This trend is consistent with Fig. 10 for $z/D_h \geq 10$. This means that the dynamics of convective mixing below $z \sim 300$ are such that the resulting RMS of the triple-jet especially in the region adjacent to and including the cold jet, falls below that of even an isothermal single-jet. In other words, just based on the RMS velocity data the

thermal mixing appears to take place (transverse to the flow of the jet) such that the turbulence is in effect "depleted" in the central region.

4.3 Temperature measurements

We next present in Figs. 12 and 13 the spanwise average temperature and its associated standard deviation profiles respectively at selected axial locations. The axial distances were selected for clarity in presentation and to correspond as much as possible to the velocity profiles. Note that at z = 20 [mm] the profile clearly indicates the presence of a central cold jet (T ~ 25.5°C) and two hot jets (T ~ 30.8°C), while in-between (to the right and left of z ~ 90) the temperature assumes the "approximate average" of 28°C over a span of 30 mm on either side of the cold jet. Near the regions of the individual jets, the temperature gradient is very sharply defined. At a distance 50 mm further downstream, at z = 70 mm, the "mixing" of the thermally-stratified streams appears well under way and the profile reflects this as the gradients (to either side) between the hot and cold jets have decreased (e.g. 100 < x < 108); that is, the temperature gradient, although still larger than at successively higher axial distances, is smaller in comparison to z = 20. By z = 180 then, the temperature gradients between the hot/cold streams are much smaller and overall, the thermal mixing brings about a "flattening" of the spanwise temperature profile. From z = 20 to 180, the axial center of the cold jet has increased in temperature (from 25.5°C) to nearly 29°C while the hot jets have decreased in temperature from 30.8°C to 29.5°C, which is a smaller absolute change than for the cold jet. The apparent reason for this is the presence of two hot jets which transfer heat to the single cold jet. Beyond z = 180 the temperature profile does not change significantly and resembles the profile at z = 180. Thus except for z = 500 we have not shown the profiles at z = 200, 300 and 400 mm.

As for the standard deviation distribution, the profile shows for example at z = 20, a "twin-peaked" profile similar to Fig. 7b for velocity while in between the jets there is a "plateau" or flat region describing temperature uniformity. At z = 30 however, the profile is already changing as the magnitude of the plateau regions increases relative to the twin-peaks of the central jet. This trend continues at z = 40. One can also see that the profile near the hot jets does not change as much as the region surrounding the cold jet. This appears to be an early indication of the thermal mixing at these lower axial locations. By z = 80, the overall fluctuation level has increased markedly and the profile itself has changed dramatically. In fact, most of the thermal fluctuations are clearly in between the hot and cold jets, while there appear to be smaller "peaks" located on the far side (see right jet, z ~ 164) of each of the hot jets. Note too that the relative width of the cold jet's core region remains fairly unchanged (compare z = 40, 80) and that a local minimum value exists up to z ~ 140 but no longer at z = 180. This means, at least qualitatively, that the thermal mixing has not yet reached (spanwise) the core of the cold jet at 80 < z < 140. This is, however, no longer the case at z = 180 where the "defect" seen at z < 140

has all but disappeared. Beyond z = 180 the profile assumes a gradually decreasing Gaussian-like distribution such that at z = 500, the magnitude is less than 1% of the average at that location.

We asserted from a hydrodynamic point of view, based on the RMS velocity data, that mixing most likely takes place over the axial span, $70 < z < 250$ ($2 < z/D_h < 7$) and in particular, in contrast to the single-jet, the mixing is especially accentuated in the region in-between the jets. We would thus expect much of the thermal convective mixing to occur *in-between* the cold and hot jets as well. We first show however, in Fig. 14 the normalized RMS value for temperature along the axial direction. This figure shows that consistent with the RMS data for velocity, the RMS for temperature reach their largest values, say over 1%, along $60 < z < 300$ mm ($1.68 < z/D_h < 8.4$). The axial span over which thermal convective mixing takes place approximately coincide as expected.

For the conditions given in this work the non-dimensional groupings, mainly the Reynolds (Re), Grashof (Gr) and Richardson ($Ri = Gr / Re^2$) numbers calculated at the mean exit temperature of 27.5°C and based on the hydraulic diameter D_h were as follows: $Re = 2.1 \times 10^4$, $Gr = 8.75 \times 10^5$ and $Ri = 1.98 \times 10^{-3}$. If the Ri-number is taken as the ratio of buoyancy to inertial forces, then conditions at the exit are dominated by forced flow. Equally the local, axial distance-based Ri-number calculated on the difference between the minimum and maximum velocity and temperature yield respectively at $z = 120$, 535 mm: $Ri (z = 120) = 6.89 \times 10^{-3}$ and 15.5×10^{-3}. So it does appear that the buoyancy force increases relatively to the inertial force from an axial location where mixing is vigorous (z = 120 mm) to where it is essentially complete (z = 535 mm). However, our flow at z =535 mm is still predominantly jet-like and not plume-like.

In Figure 15, we presented an iso-contour plot of the estimated turbulent heat flux distribution that we derived from separate calculations of the RMS for velocity, *w'*, and temperature, *t'*, both as a function of (x,z). We previously noted true nature of *w'* due to the inclination of the ultrasound transducer. It is by coincidence that the spanwise turbulent heat flux is the one calculated and is also the quantity which may hold more significance in terms of evaluating the thermal mixing. That is, if the spanwise mixing is efficient and thus the heat energy is dissipated, the thermal striping impact is lessened on any solid boundary which the flow encounters. In other words, at a given axial location, the uniformity in the spanwise temperature distribution is a measure of the thermal mixing which has taken place below it. So in spite of the compromises made in matching the velocity and temperature fields, the figure strongly supports our view that there is significant *convective mixing* of thermal energy contained in the two heated jets mostly to the cold jet. This is carried out for an average exit nozzle velocity of 0.5 m/s and $\Delta T = T_{hot\ jet} - T_{cold\ jet} = 5°C$, along an axial span $70 \sim z \sim 160$ mm or when non-dimensionalizing with the exit nozzle's hydraulic diameter, $z/D_h \sim 2.0$ to 4.5. In addition, the corresponding spanwise width where most of this mixing takes place is $x/D_h \sim 2.25$ centered about the axis of the central (cold) jet.

Finally in Fig. 16 we have shown the axial distribution of frequency of the first six peaks ranked in terms of their "power" which is a measure of the turbulent kinetic energy associated with the flow. It seems clear that there are two frequencies, one at approximately 2.25 HZ and the other at 0.7 Hz, dominant in the flow with a transition from the higher to lower frequency at roughly $z = 300$. Additionally the frequency mode $f = 2.25$ Hz is established within the first $z < 80$ mm from the jet exits and coincides with the span over which thermal mixing is thought to occur. It is therefore likely that especially for a low Prandtl number fluid like sodium ($Pr \sim 0.001$) that both hydrodynamic and thermal fluctuations are characterized for a flow of this type (and under similar conditions) by frequencies of order 2 Hz. That is, if our water data primarily yields frequencies 0.7 and 2.25 Hz, with the large thermal diffusivity (and smaller viscosity) of sodium we would expect "thermal frequencies" in a similar range. In fact these two frequencies are within the range observed by Brunings (1982), 0.1 to 2.0 Hz, who measured temperature fluctuations in a thermal striping experiment using sodium. We also mention in closing that the transition from 2.25Hz to 0.7 Hz signifies a change in the nature of the flow. Although we plan to investigate this further the transition at $z = 300$ roughly corresponds to the axial location beyond which Fig. 5 and other video-images suggest a composite single-jet like structure with a virtual origin for the triple-jet. It is also the approximate axial location where the triple-jet's RMS reaches a quasi-constant magnitude equivalent to that of the single-jet.

5

Conclusions

An experiment investigating the thermal-hydraulic mixing of three quasi-planar, vertically flowing (water) jets was conducted. In the experiment the central jet was at a lower temperature than the two adjacent jets which were at the same temperature. The jets flowed into a large volume of water initially at the central jet's temperature. The average exit velocity (and flowrate) of the three jets was equal. Velocity measurements were taken using an ultrasound Doppler velocimeter while temperature data were taken from an traversed array of thermocouples. The velocimeter yielded velocity profiles consisting of 128 points along its measurement line which were constructed from the echo signals received from ultrasound reflecting particles moving with the flow. Except for some apparent difficulty in the echo signal processing (amplification) in the region close to the transducer both single- and triple-jet configurations yielded satisfactory velocity data. In fact a plot of the centerline decay velocity of our single-jet was in agreement with data extracted from past investigations. In addition velocity measurements yielded a measure of the flow fluctuations; that is, the standard deviation associated with the average velocity provided, in addition to the temperature data, a means of evaluating the turbulent nature of the flow and the mixing process.

As for the triple-jet some expected similarities to the single-jet were observed, but generally the triple-jet exhibited an elevated level of fluctuations associated with the flow expressed in terms of the standard deviation of the velocity signal. In fact in comparison to the single-jet, normalized RMS values were as much as 20 times as large in the region between the buoyant and non-buoyant (central) jet. Beyond $z \sim 300$ ($z/D \sim 10$) however, due in part to thermal convective mixing of the jets, RMS of the single, isothermal jet exceeded the triple-jet. We thus partially concluded that for equal average jet exit velocities of $U_{avg} = 0.5$ m/s and a central-to-adjacent jet temperature difference $\Delta T = 5°$ (30°C and 25°C) most of the convective mixing between the thermally-stratified jets occurs over an axial distance of $z/D_h \sim 2.0$ to 4.5 where D_h is the hydraulic diameter of the exit nozzle. The mixing was on-average centered about the axis of the central jet and span a width, $x/D_h \sim 2.25$. In fact most of the convective mixing takes place in the region defined by the edges of the central jet and the right and left edges of the adjacent jets; that is, in the regions in-between the cold and hot jets.

Finally a brief look into the spectral nature of the measured data revealed two primarily frequencies associated with the flow, these being a dominating frequency of 2.25Hz established within the first 80 mm from the exit and a lower frequency of 0.7 Hz appearing beyond a transition at approximately $z \sim$ 300 mm downstream.. From these results we were led to reason that for a low Prandtl number fluid such as sodium temperature fluctuations would more than likely occur at similar frequencies.

Acknowledgments

References

Betts C; Bourman C; Sheriff N (1983) Thermal striping in liquid metal cooled fast breeder reactors, 2nd Int'l Topical Mtg. on Nuclear Reactor Thermal Hydraulics, NURETH-2, Santa Barbara, CA, USA, vol. 2, 1292-1301

Brunings J E (1982) LMFBR thermal-striping evaluation, Interim report, Rockwell International Energy Systems Group, Canoga Park, CA, USA , Research Project 1704-11, EPRI-NP-2672

Cheremisinoff N P (1986) ed. In: Encyclopedia of Fluid Mechanics, Dynamics of Single-Fluid Flows and Mixing, vol. 2, Houston, USA: Gulf Publishing Co.

Moriya S; Ushijima S; Tanaka N; Adachi S; Ohshima I (1991) Prediction of Thermal Striping in Reactors. Int'l Conf. Fast Reactors and Related Fuel Cycles, Kyoto, Japan, vol. 1, 10.6.1 - 10.6.10, Oct. 28 - Nov. 1

Muramatsu T (1994) Development of thermohydraulics computer programs for thermal striping phenomena, Specialists meeting on correlation between material properties and thermohydraulics

conditions in LMFRs. IAEA Working Group on Fast Reactors, IWGFR/90, Aix-en-Provence, France, November 22-24

Gebhardt B; Jaluria Y; Mahajan R L; Sammakia B (1988) In: Buoyancy-Induced Flows and Transport, Reference Edition, New York: Hemisphere Publishing Corporation

Takeda Y (1986) Velocity profile measurement by ultrasound Doppler shift method, Int. J. Heat and Fluid Flow. 8:313-318

Takeda Y (1991*a*) Development of an ultrasound velocity profile monitor, Nucl. Eng. Design. 126: 277

Takeda Y ; Kobayashi K (1991*b*) Ultrasonic flow visualization of transient behavior of Taylor vortex flow. In: Experimental and Numerical Flow Visualization, ASME FED-128, 231

Tenchine D; Nam H-Y (1987) Thermal hydraulics of co-axial sodium jets. Am. Inst. Chem. Engrs. Symp. Ser. 83(257):151-156

Tenchine D ; Moro J-P (1995) Comparative analysis of sodium and air mixing jets experiments. 8th IAHR Working Group Mtg. Adv. Nucl. React. Thermohydraulics, Rez, Czech Rep., June 13-15

Ultrasound Velocity Profile monitor (1992) Model X-1, Met-Flow SA, Lausanne, Switzerland

Wood D S (1980) Proposal for design against thermal striping. Nuclear Energy. 19(6): 433-437

Figure 1. Schematic of experimental loop.
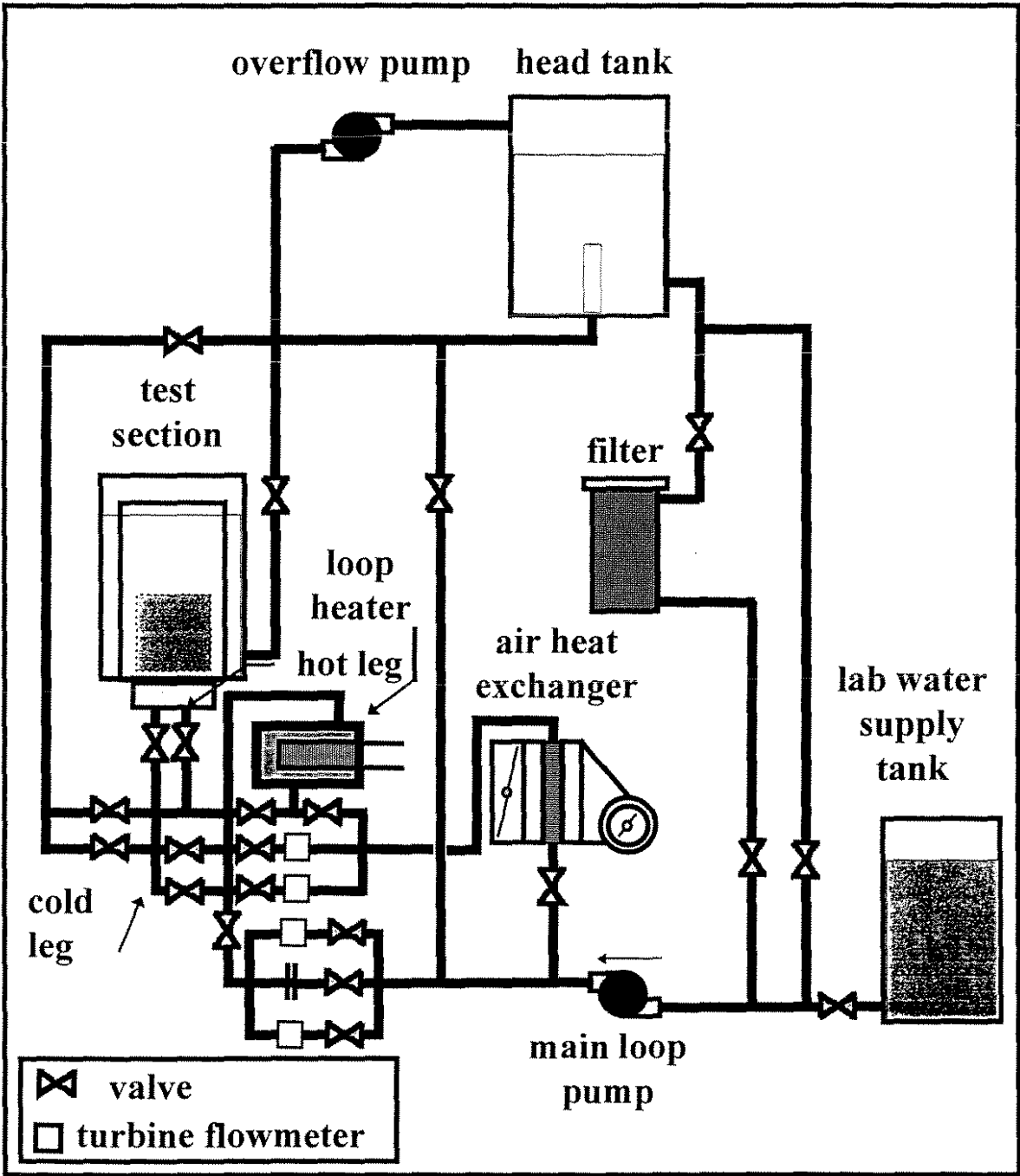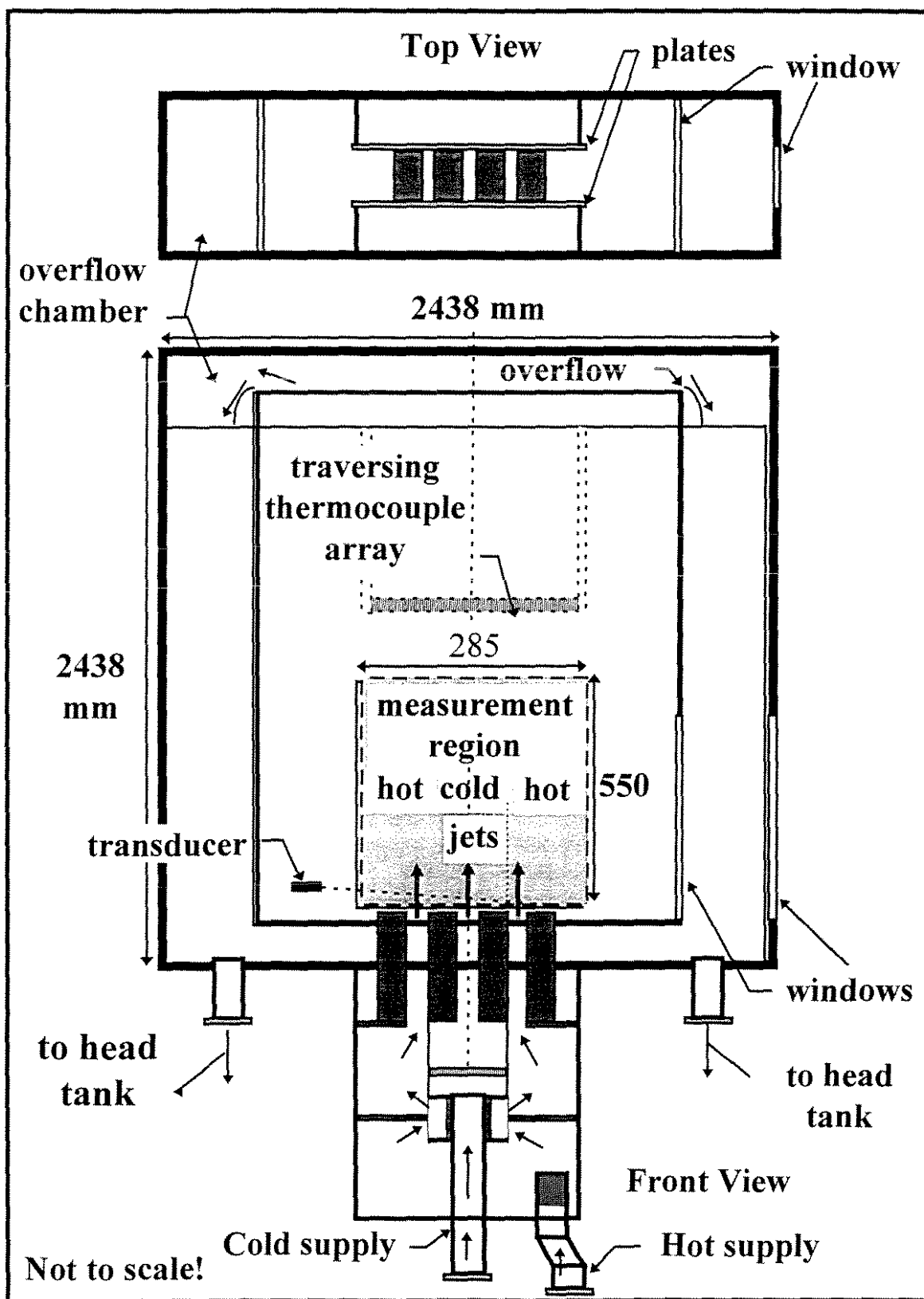
Figure 2. Schematic of test section.
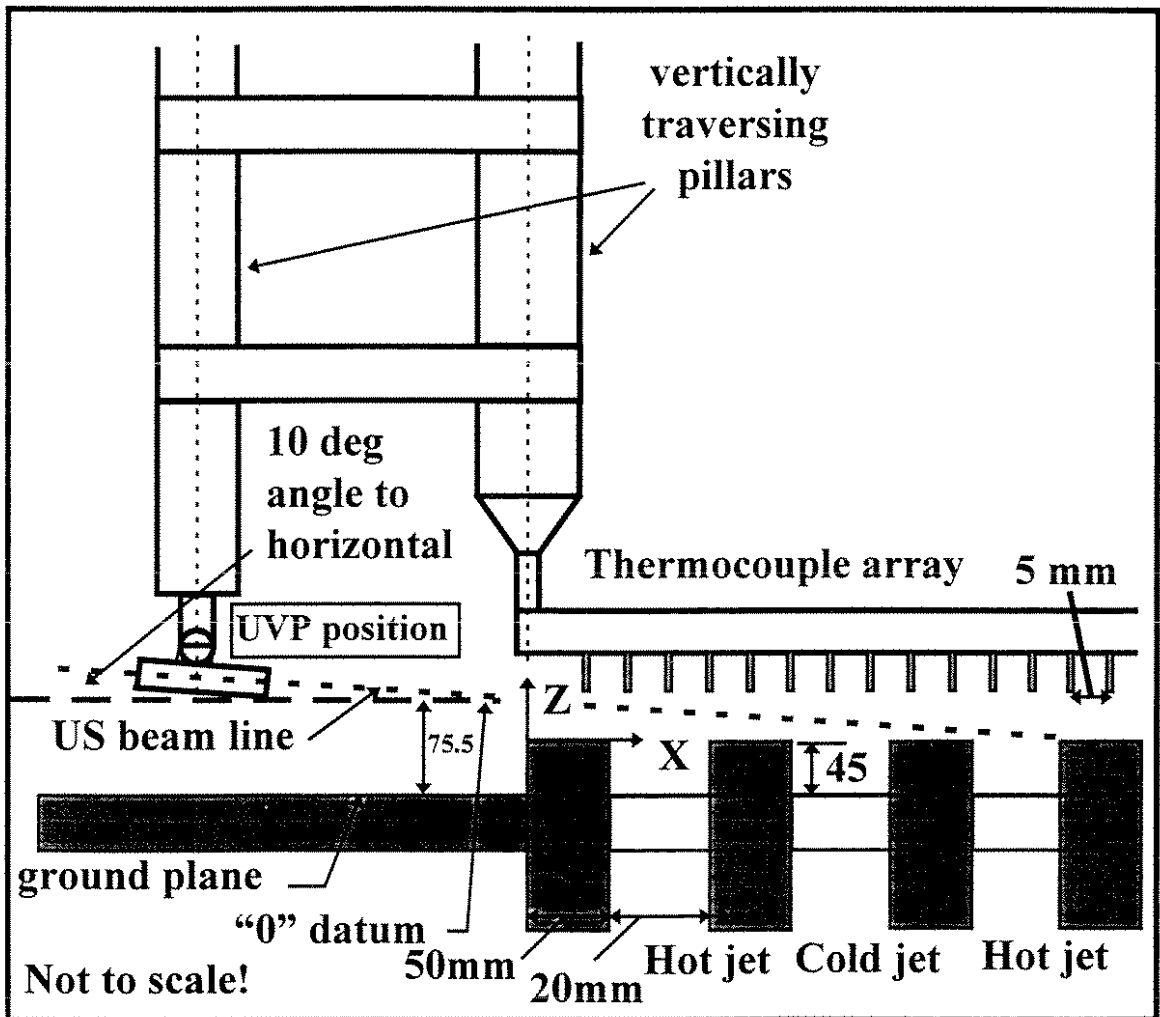
Figure 3. Schematic of instrumentation set-up. Close-up of the UVP transducer orientation and traversing thermocouple array.
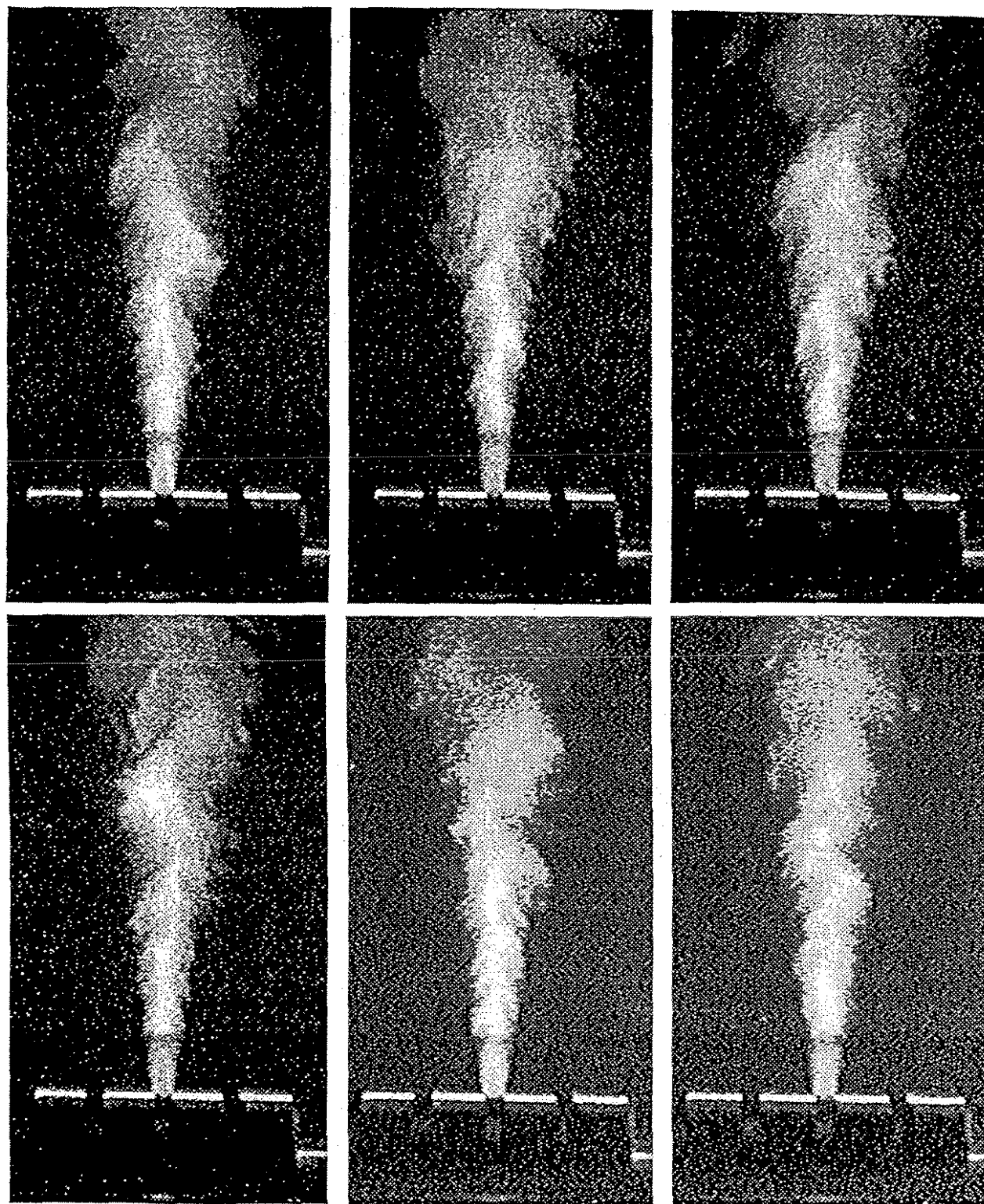
Figure 4. A sequence of 6 snapshot images digitized from video of the single-jet.
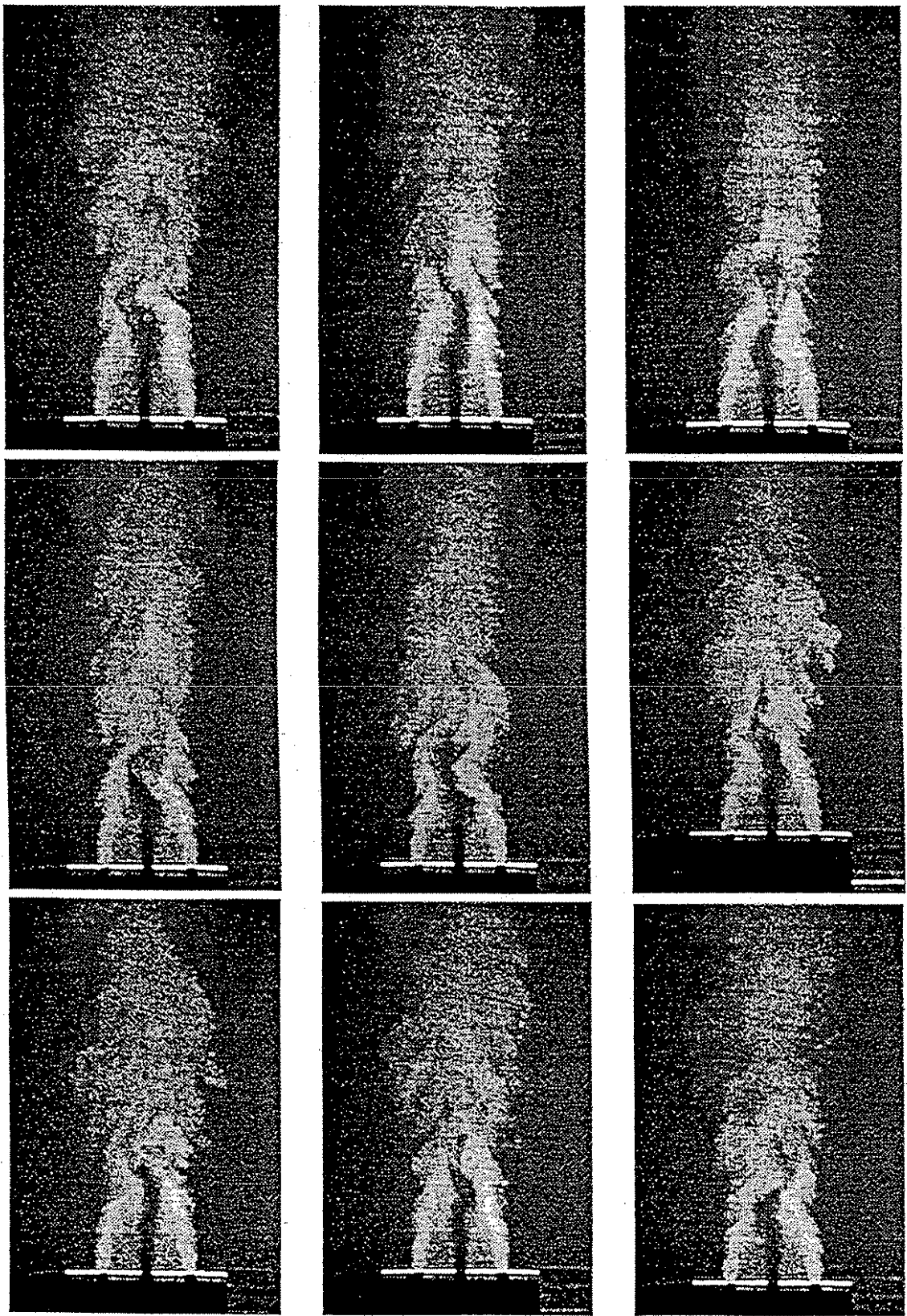
Figure 5. A sequence of 9 snapshot images digitized from video of the triple-jet.

self-preserved
velocity profile in
the developed

$U_{ctr,max}$

profile in the
mixing layer or
developing region

entrainment
occurs all
along the
edge

$U_{ctr,max}$

mixing layers

$U_0=U_{ctr,max}$

entrained
flow
core of the jet
jet exit

z

x

flat, square or
top-hat velocity
profile at exit

jet exit nozzle

hydraulic
diameter, D_h
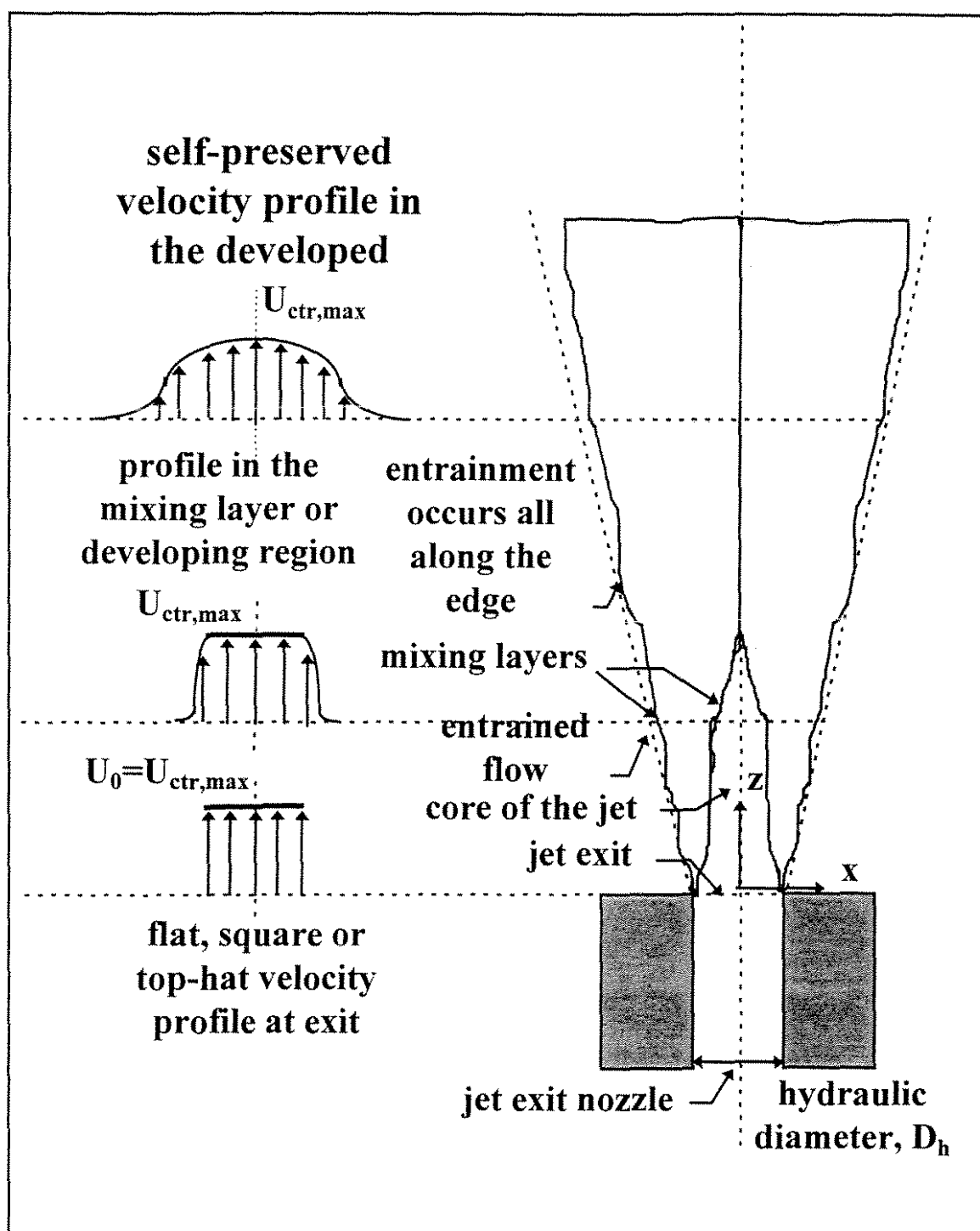
Figure 6. Idealized velocity profiles at 3 axial locations and a qualitative sketch of a plane turbulent jet.
Cf. Tennekes and Lumley.
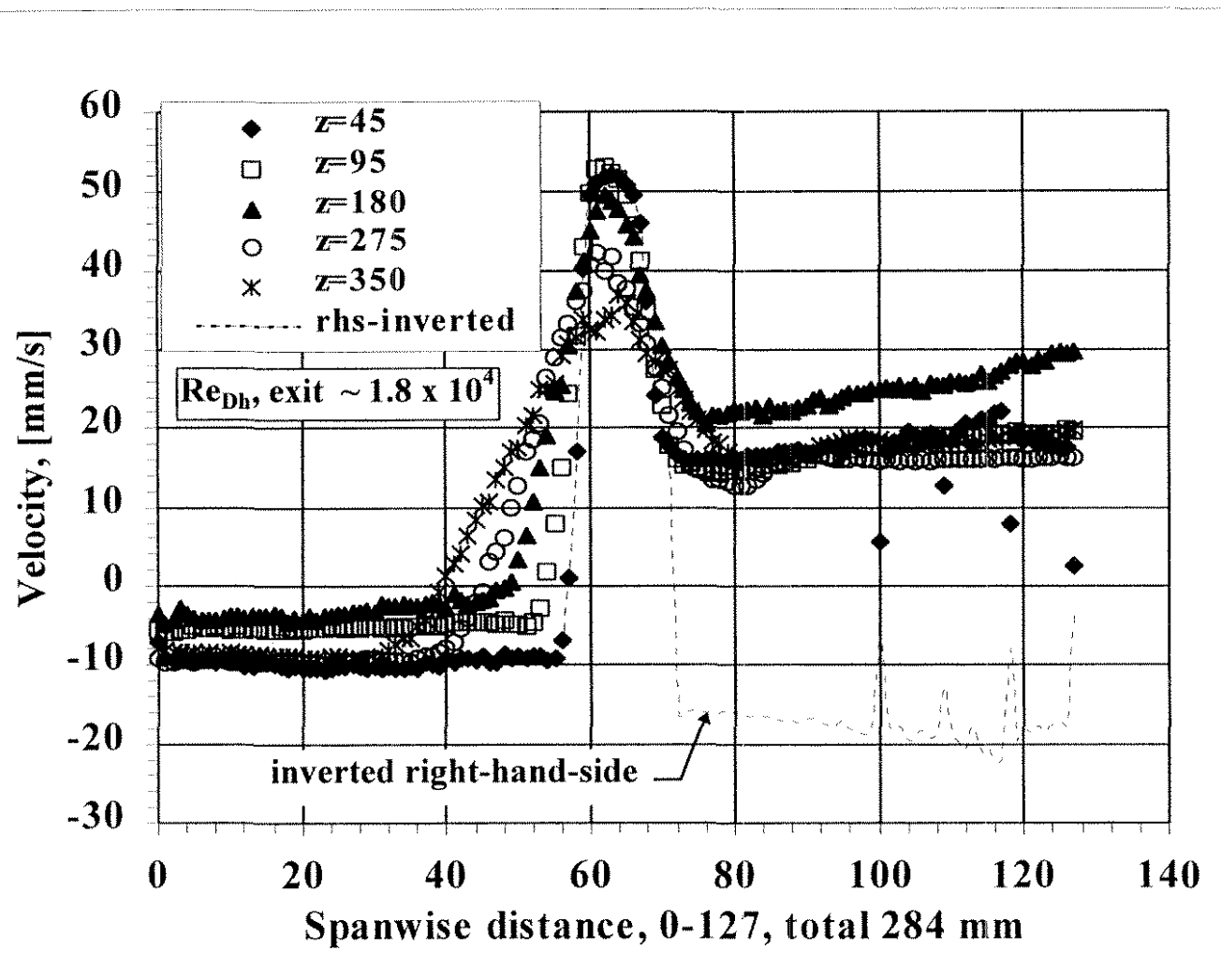
Figure 7a). Average velocity profile of the single-jet at selected axial locations.
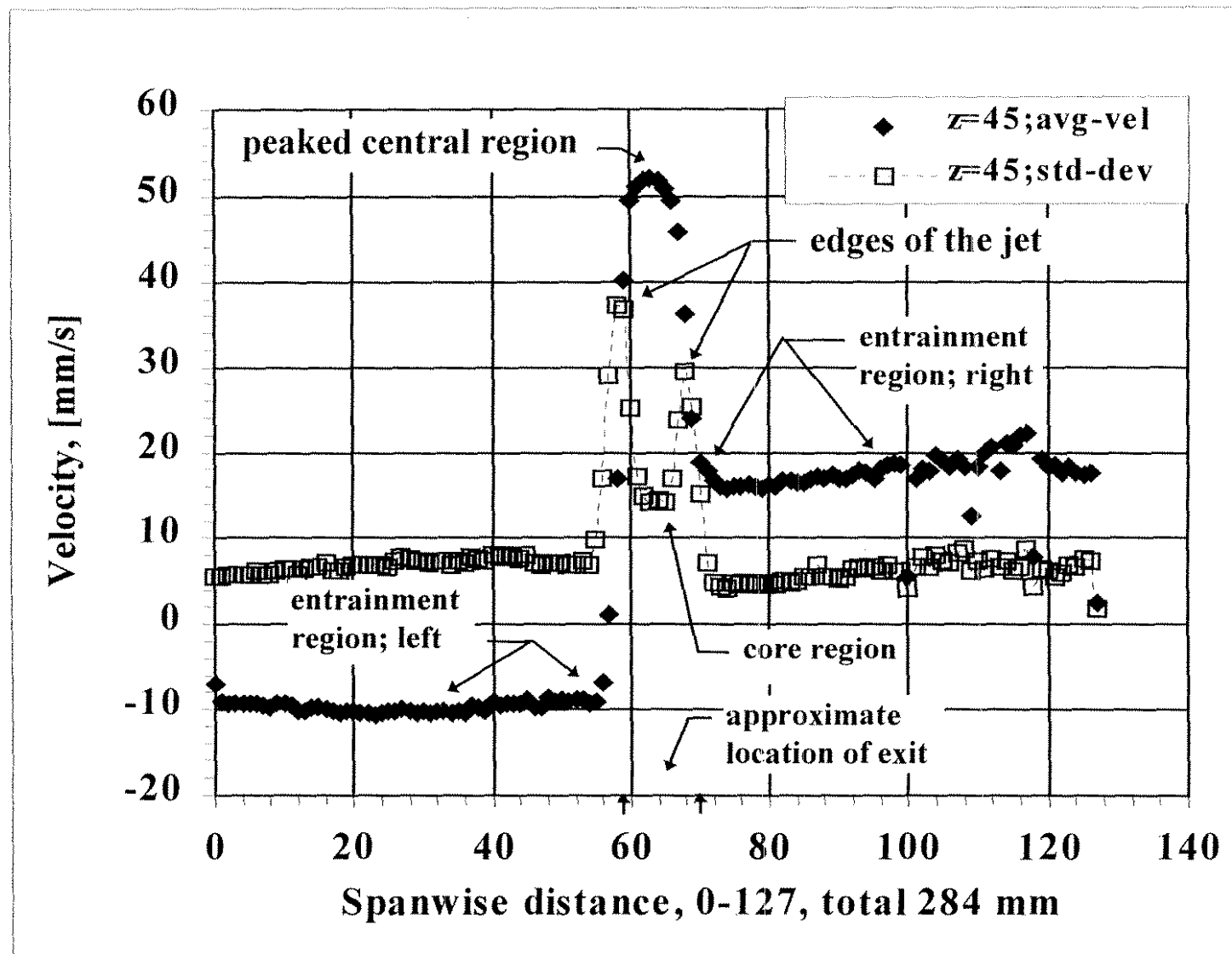
Figure 7b). Average velocity and standard deviation profiles of the single-jet at selected axial distances.
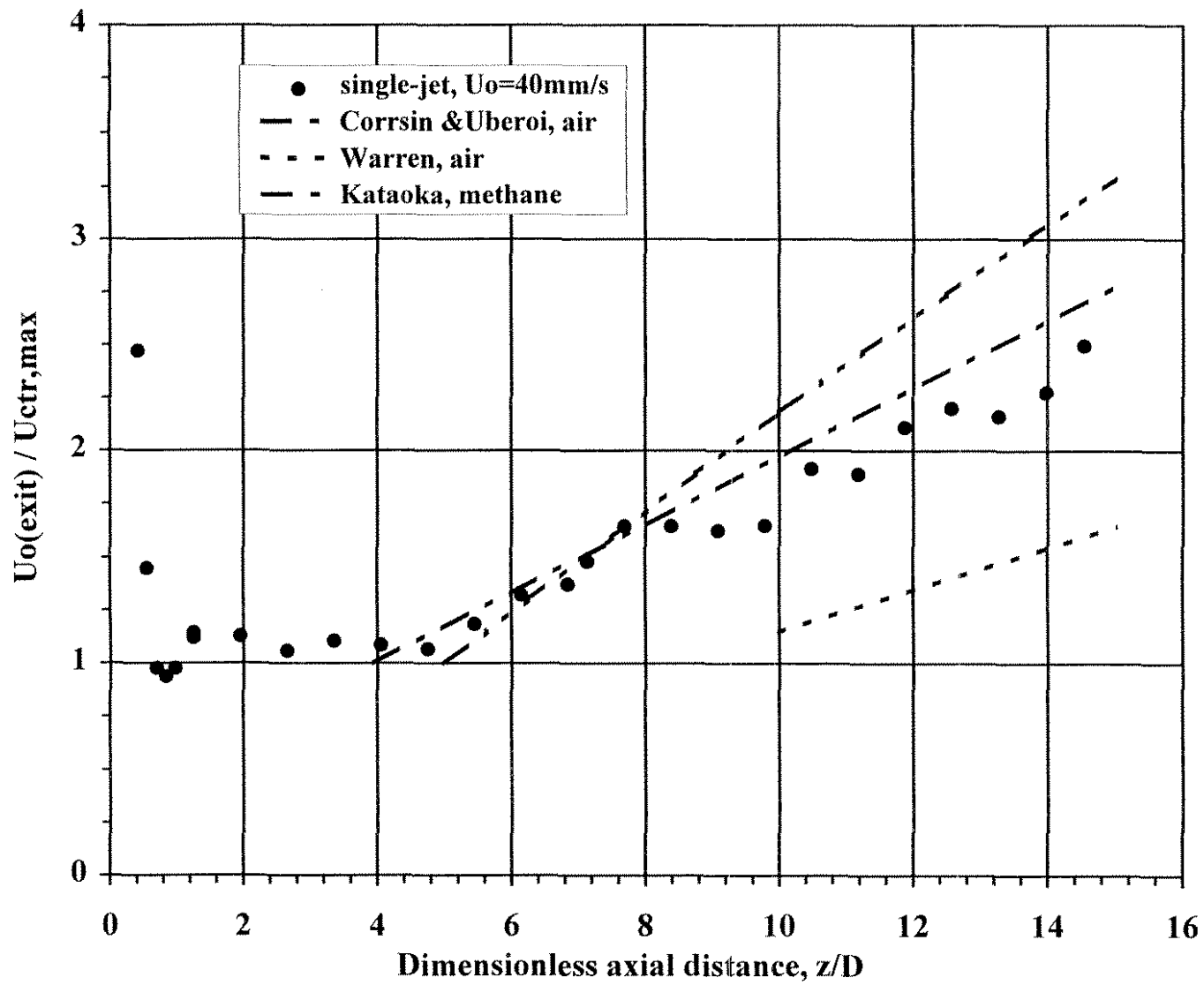
Figure 8. Axial decay of centerline velocity; a comparison of single-and triple-jet data with past data.
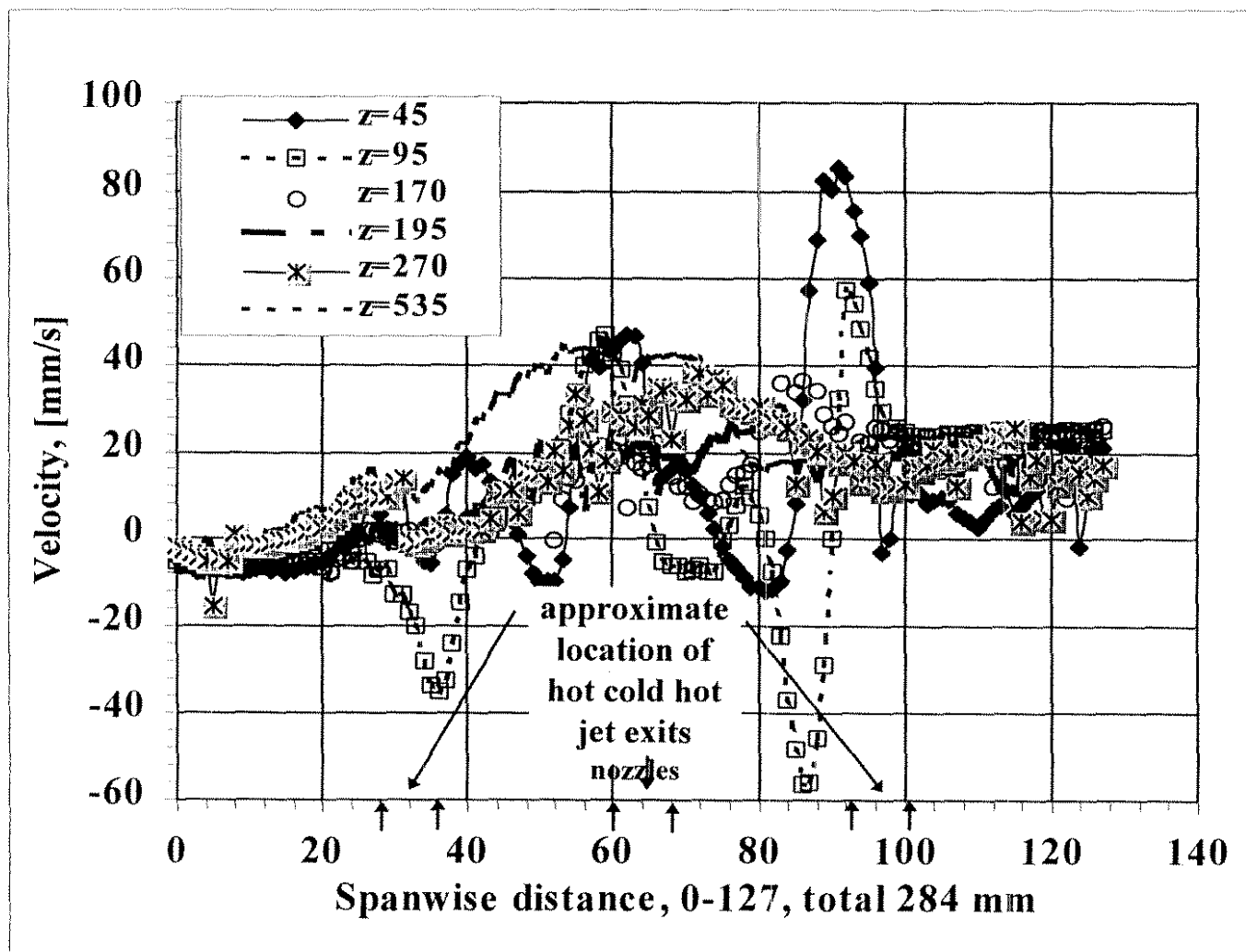
Figure 9a). Average velocity profile of the triple-jet at selected axial locations.
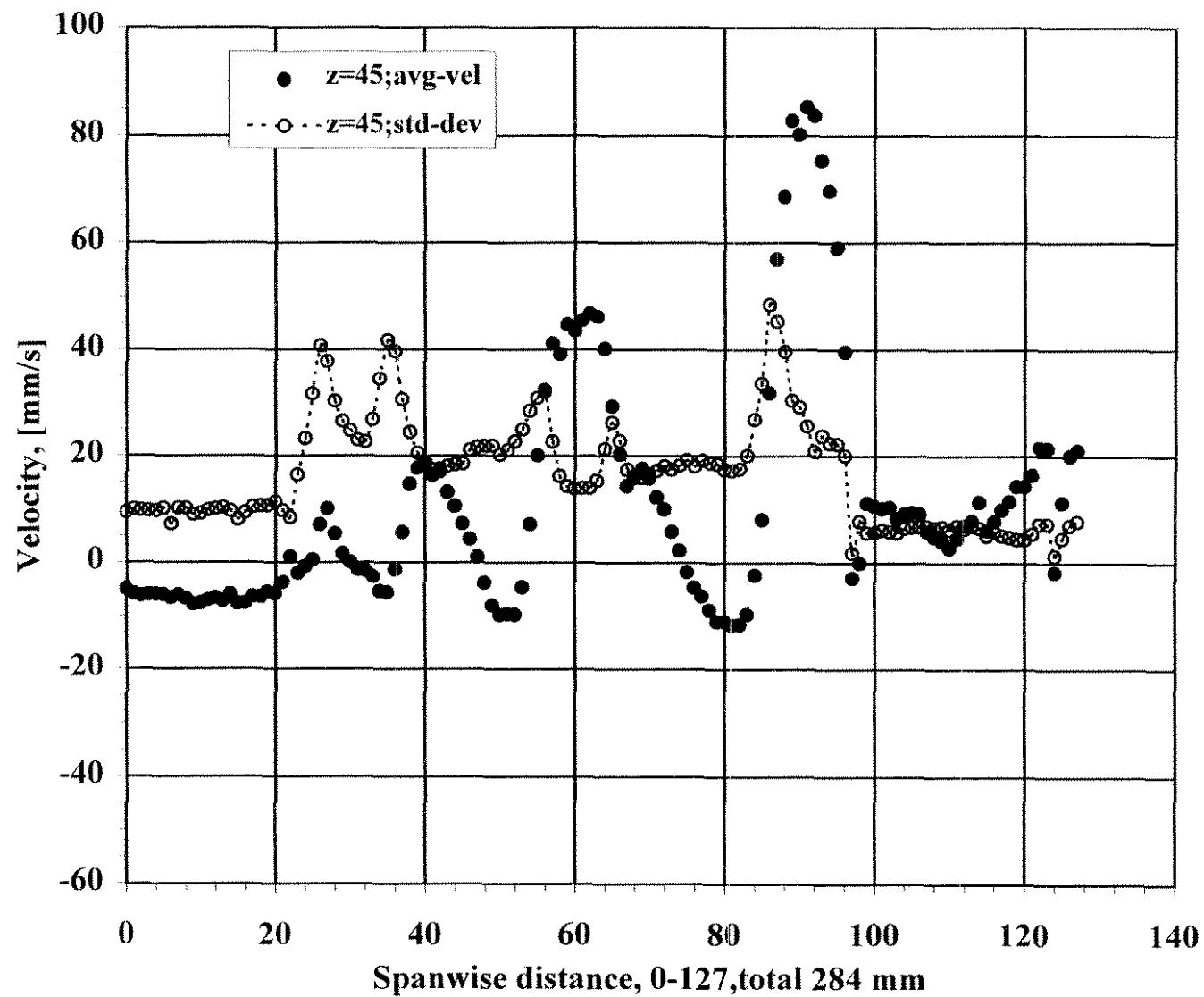
Figure 9b). Average velocity and standard deviation profiles of the triple-jet at selected axial locations.
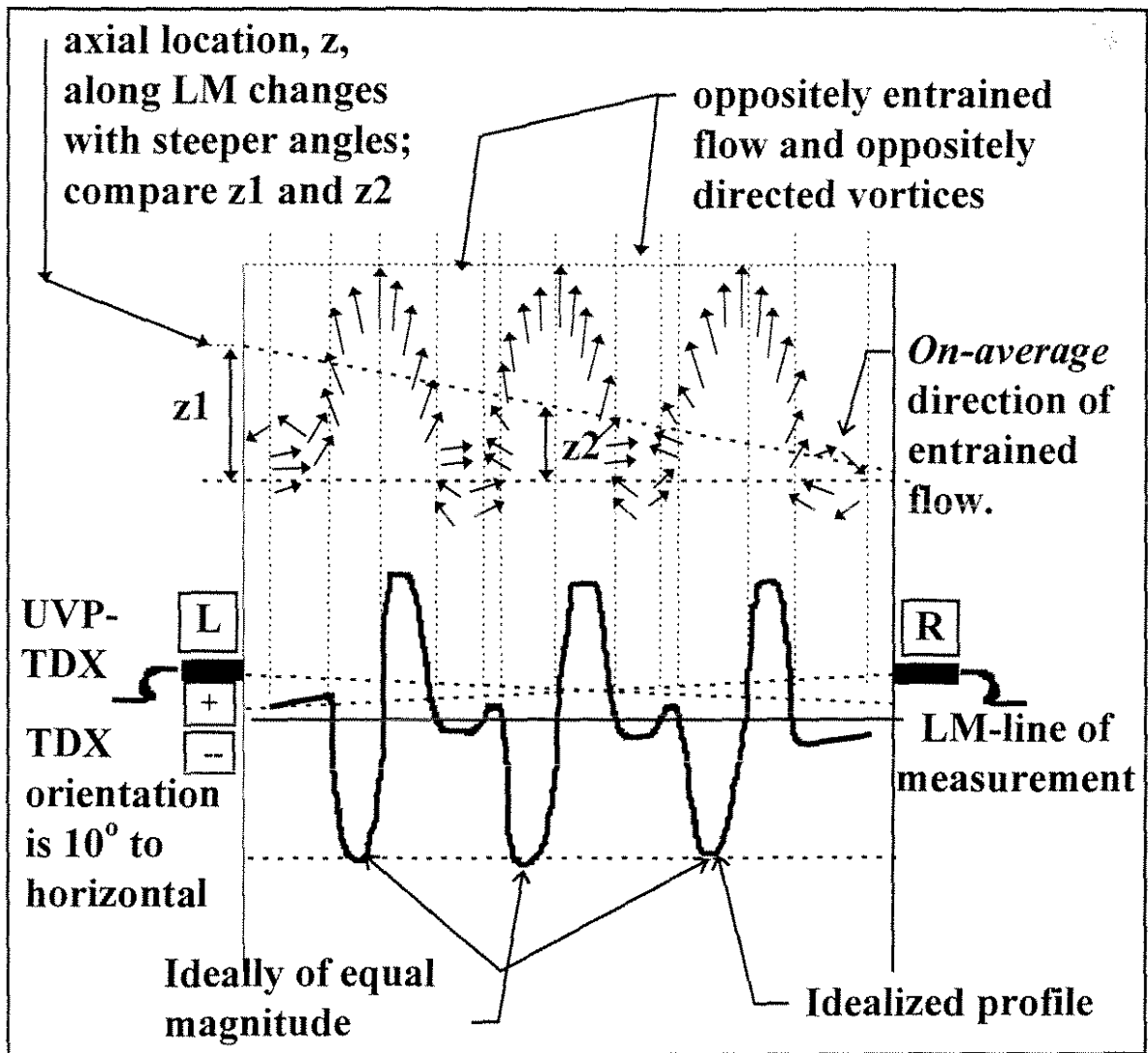
Figure 9c). Qualitative sketch of idealized triple-jet velocity profile and features.
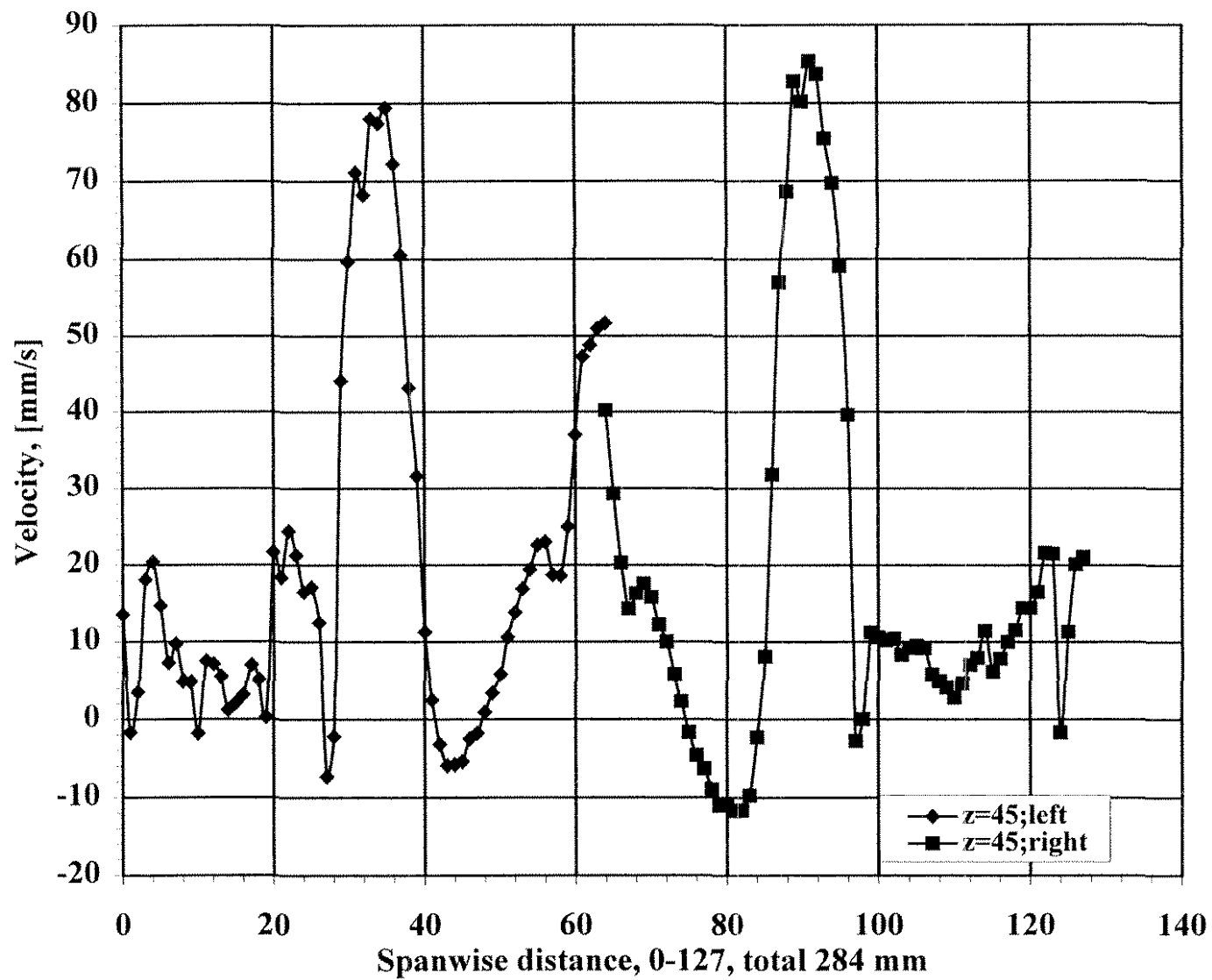
Figure 9d). Composite average velocity profile of triple-jet.
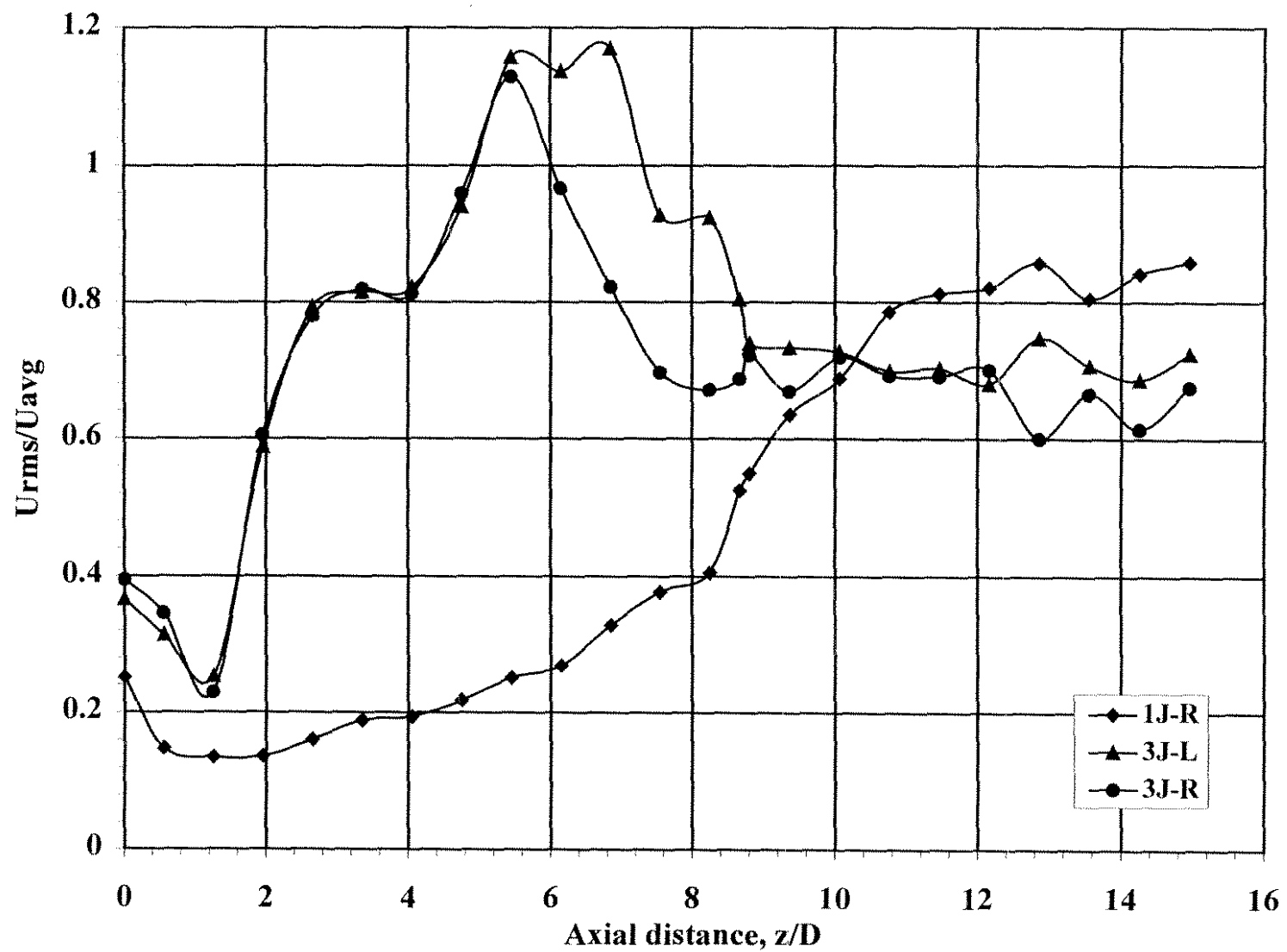
Figure 10. Comparison of the normalized RMS for velocity versus axial distance, z/D, of single- and triple-jets.
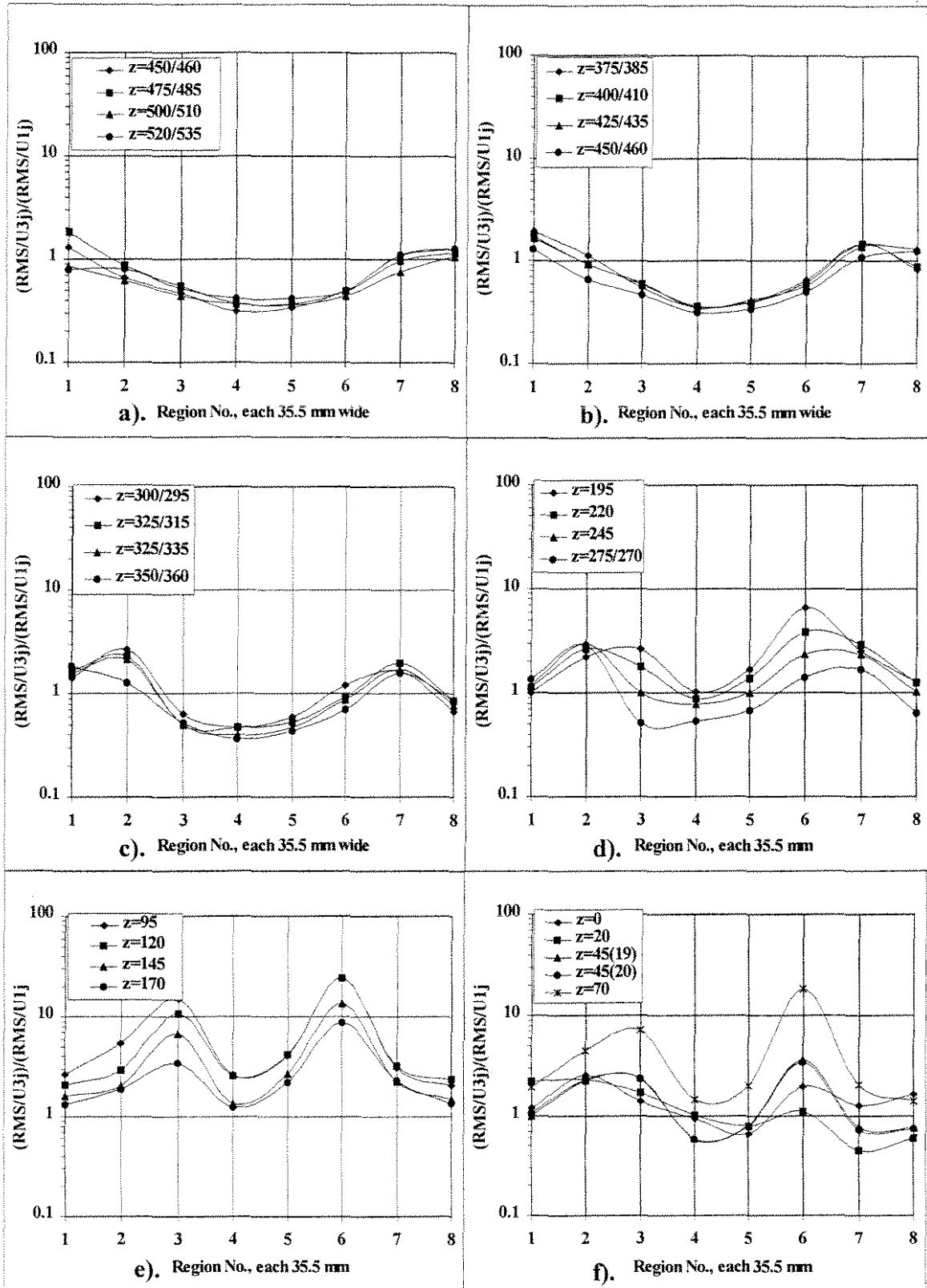
Figure 11a) - f). Spanwise distribution of the ratio of normalized RMS of the triple-jet to the single-jet as averaged regionally (1-8) and with the axial distance as a parameter.
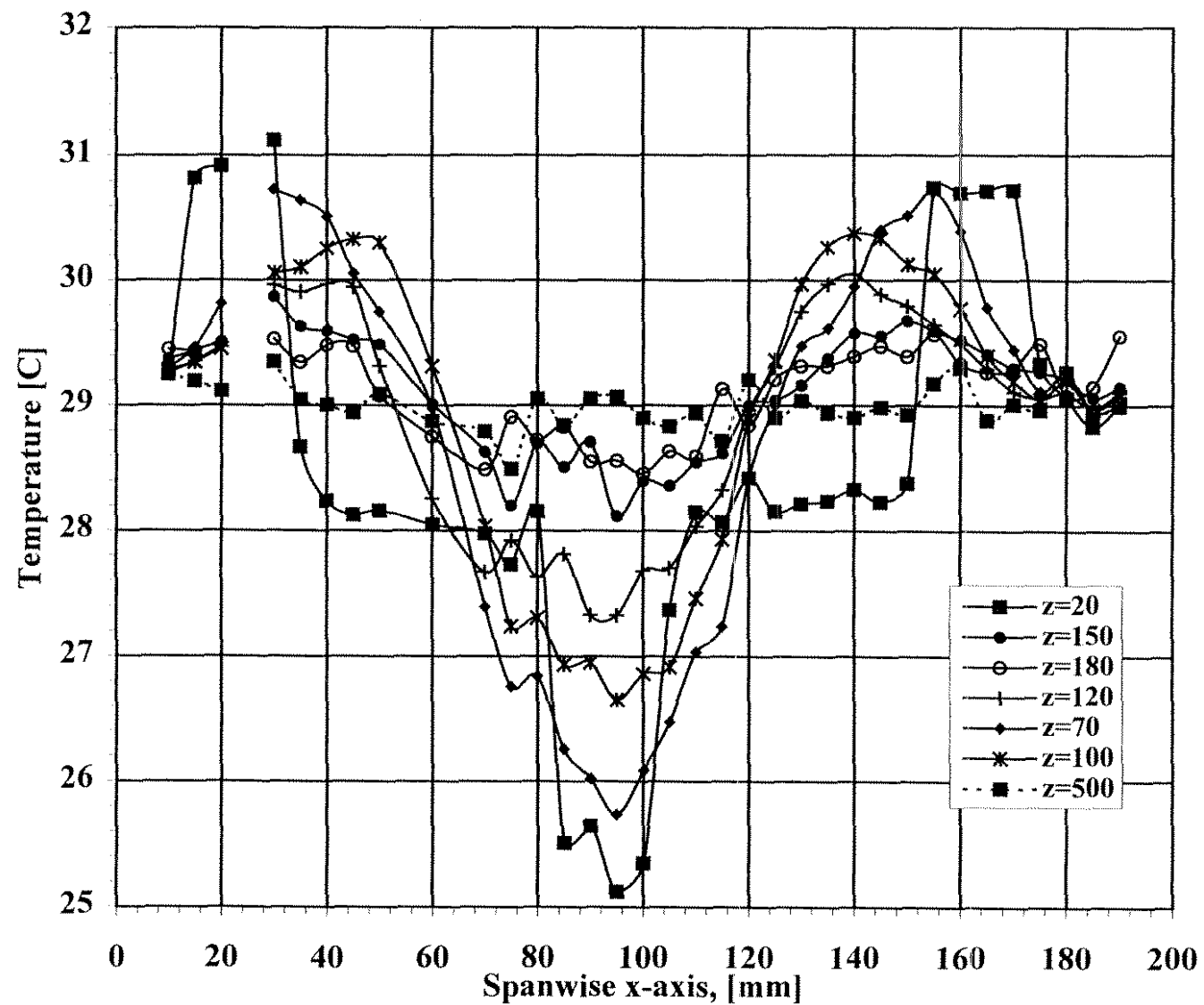
Figure 12. Spanwise temperature distribution of the triple-jet at selected axial locations.
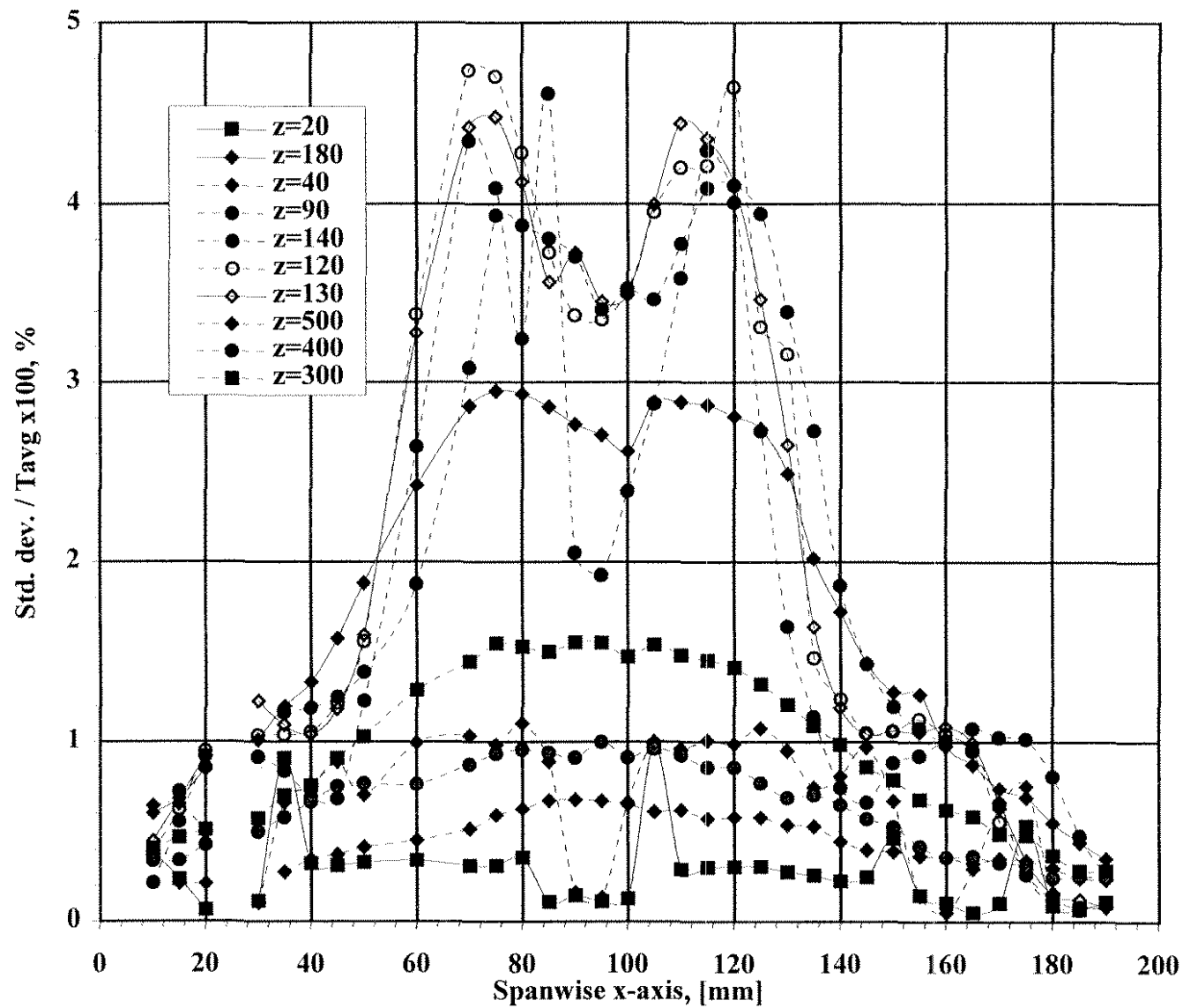
Figure 13. Spanwise standard deviation of temperature of the triple-jet at selected axial locations.
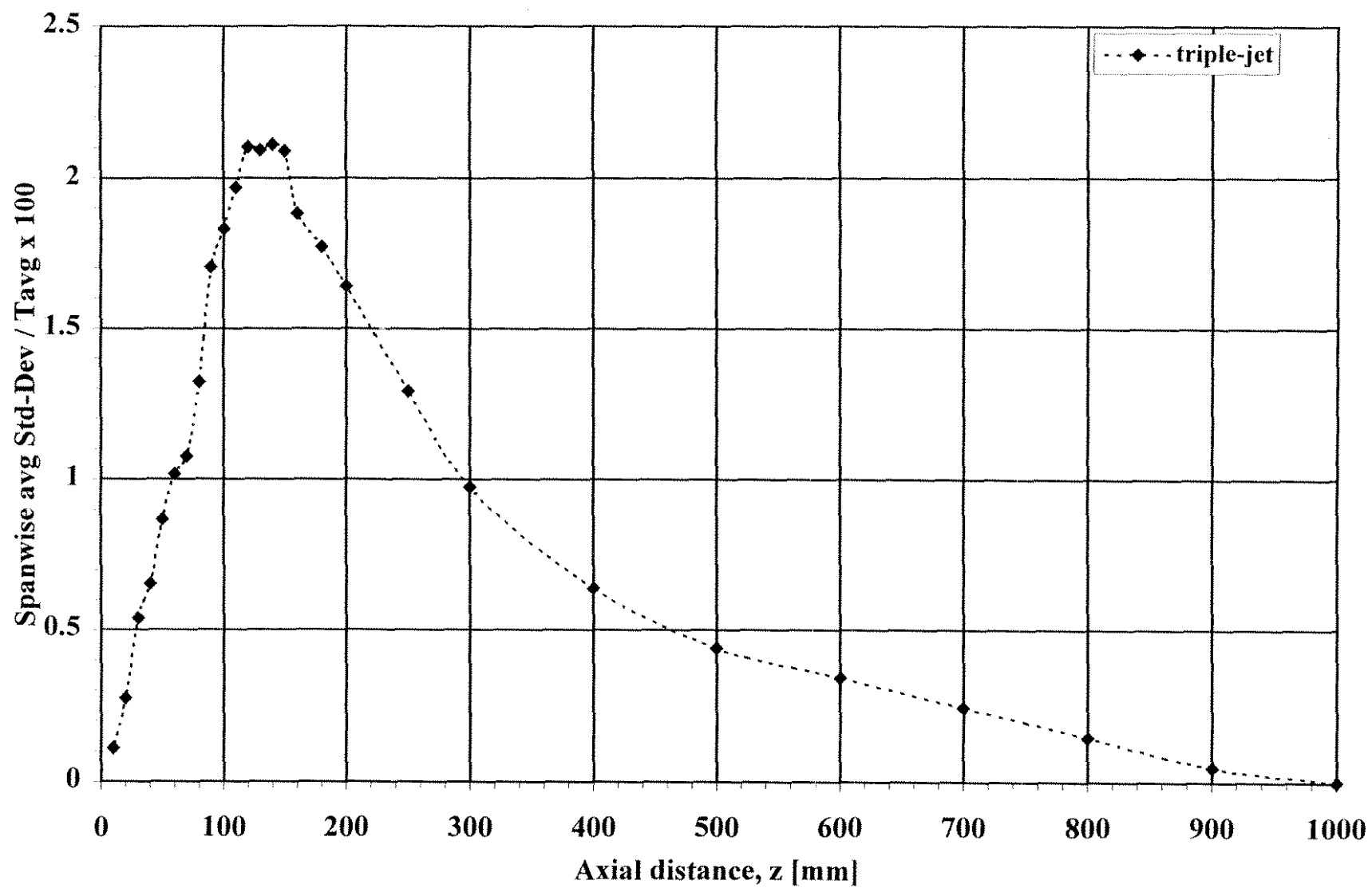
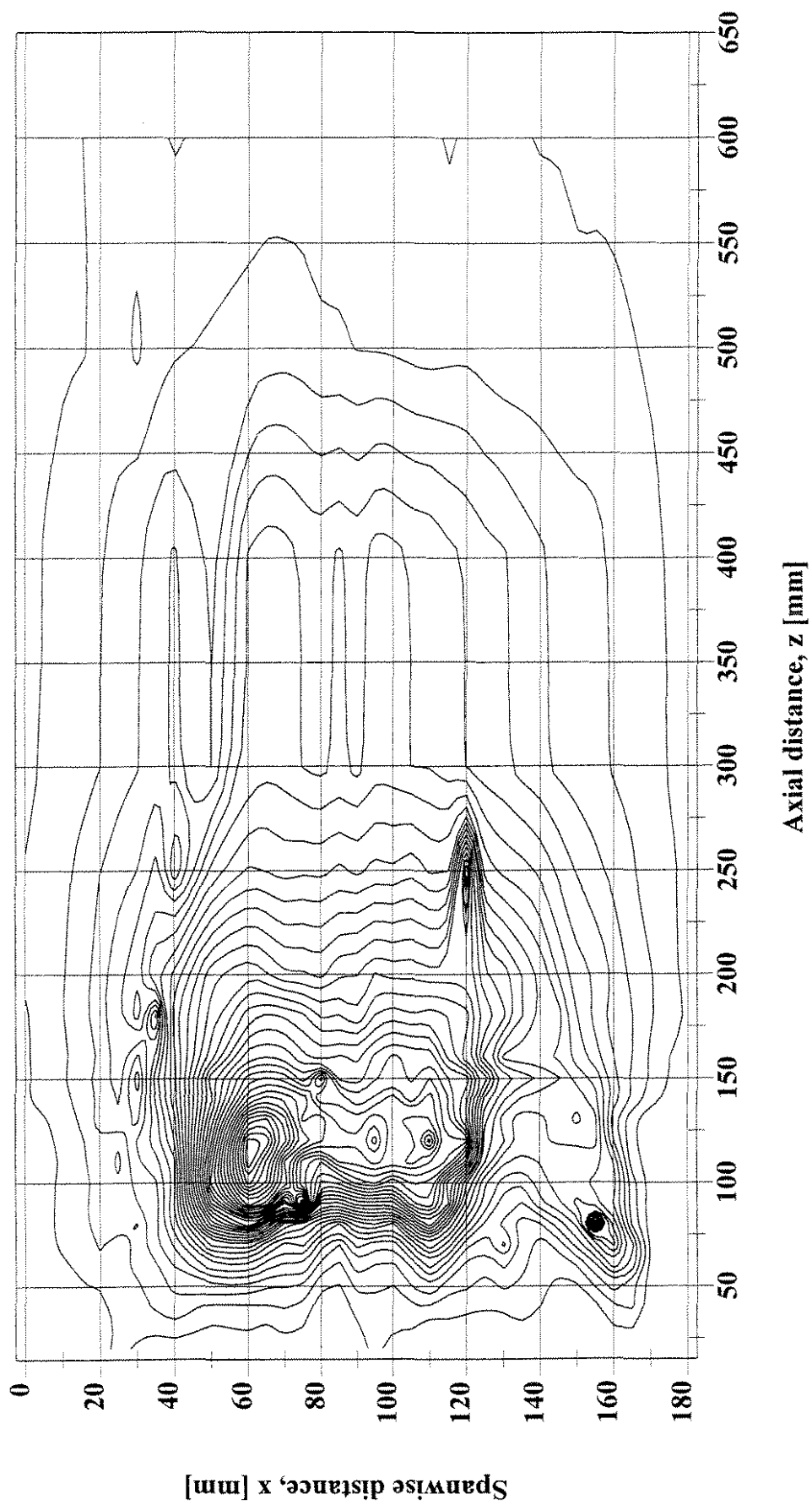Figure 14. Average standard deviation of temperature as normalized by the average versus axial distance.

Figure 15. Estimated turbulent heat flux distribution, (scale 0-360).
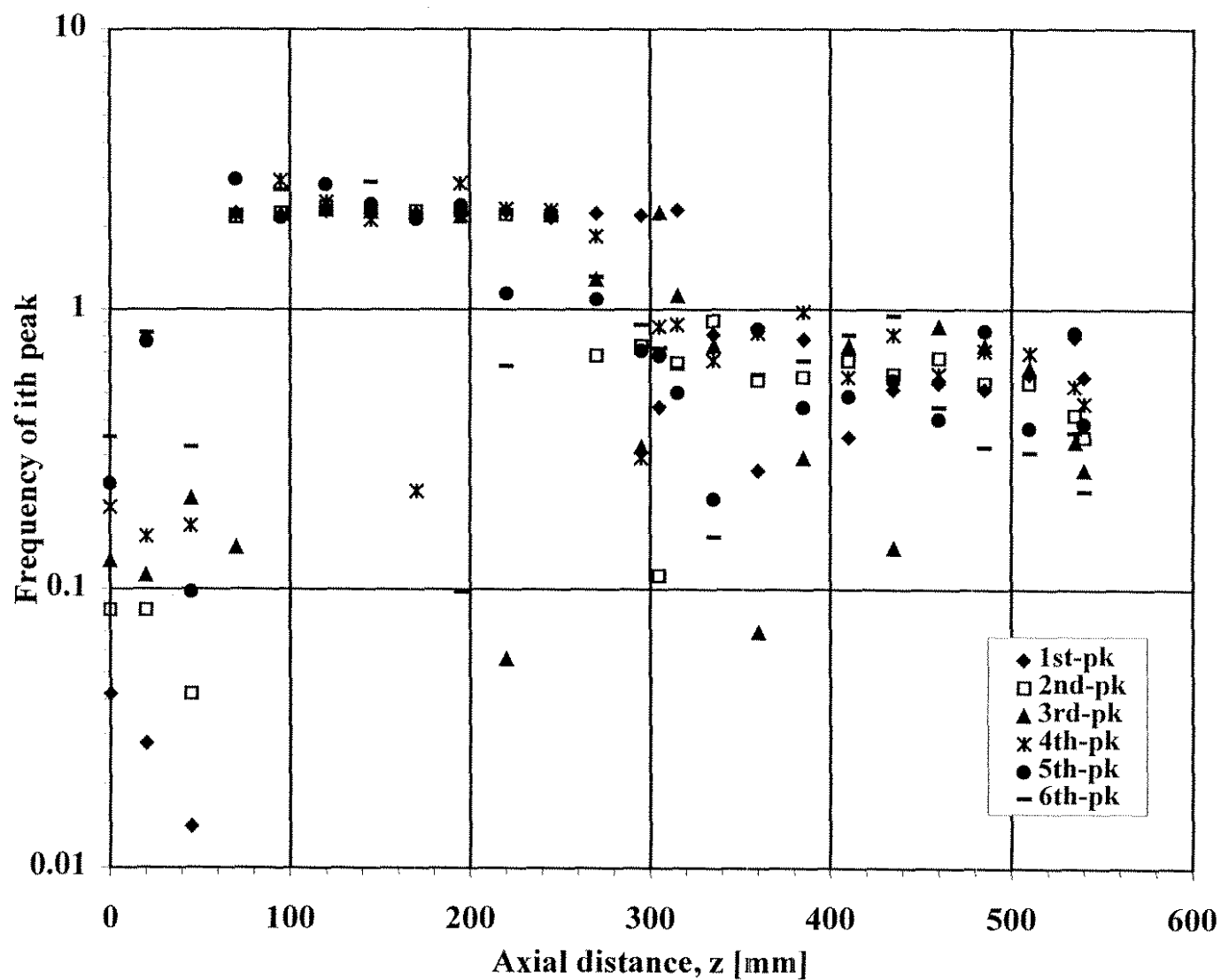
Figure 16. The frequency of the first 6 peaks based on power of the peak versus the axial distance.